

# Efficient simulation of non-classical liquid–vapour phase-transition flows: a method of fundamental solutions

Anirudh S. Rana<sup>1,†</sup>, Sonu Saini<sup>1</sup>, Suman Chakraborty<sup>2</sup>, Duncan A. Lockerby<sup>3</sup> and James E. Sprittles<sup>4</sup>

<sup>1</sup>Department of Mathematics, BITS Pilani, Pilani Campus, Rajasthan, India

<sup>2</sup>Department of Mechanical Engineering, Indian Institute of Technology Kharagpur, India

<sup>3</sup>School of Engineering, University of Warwick, Coventry CV4 7AL, UK

<sup>4</sup>Mathematics Institute, University of Warwick, Coventry CV4 7AL, UK

(Received 9 October 2020; revised 9 March 2021; accepted 26 April 2021)

Classical continuum-based liquid–vapour phase-change models typically assume continuity of temperature at phase interfaces along with a relation which describes the rate of evaporation at the interface (Hertz–Knudsen–Schrage, for example). However, for phase-transition processes at small scales, such as the evaporation of nanodroplets, the assumption that the temperature is continuous across the liquid–vapour interface leads to significant inaccuracies (McGaughey *et al.*, *J. Appl. Phys.*, vol. 91, issue 10, pp. 6406–6415; Rana *et al.*, *Phys. Rev. Lett.*, vol. 123, 154501), as might the adoption of classical constitutive relations that lead to the Navier–Stokes–Fourier (NSF) equations. In this paper, to capture the notable effects of rarefaction at small scales, we adopt an extended continuum-based approach utilising the coupled constitutive relations (CCRs). In CCR theory, additional terms are invoked in the constitutive relations of the NSF equations originating from the arguments of irreversible thermodynamics as well as being consistent with the kinetic theory of gases. The modelling approach allows us to derive new fundamental solutions for the linearised CCR model, to develop a numerical framework based upon the method of fundamental solutions (MFS) and enables three-dimensional multiphase micro-flow simulations to be performed at remarkably low computational cost. The new framework is benchmarked against classical results and then explored as an efficient tool for solving three-dimensional phase-change events involving droplets.

**Key words:** non-continuum effects, condensation/evaporation, kinetic theory

† Email address for correspondence: [anirudh.rana@pilani.bits-pilani.ac.in](mailto:anirudh.rana@pilani.bits-pilani.ac.in)

## 1. Introduction

When a liquid evaporates it loses energy, this is why sweating cools us down. Evaporation is an effective cooling mechanism widely employed by nature, for example, as a body-temperature control for mammals (Sherwood 2005), and in engineering applications, such as spray drying, spray cooling and microelectronics cooling (Dhavaleswarapu, Murthy & Garimella 2012; Ling *et al.* 2014; Plawsky *et al.* 2014). The use of pot-in-pot coolers by mankind can be tracked back to Bronze Age civilisation (Evans 2000); a device that relies on the principle of evaporative cooling.

The description of phase-transition processes at microscale and nanoscale is intriguing, mainly owing to the inability of classical continuum theories to accurately capture the rarefied vapour-flow characteristic. Specifically, as the representative physical length scale ( $\ell$ ) of the flow becomes comparable to the mean free path ( $\lambda$ ) in the vapour, i.e. the Knudsen number ( $Kn = \lambda/\ell \approx 1$ ) (Bird 1994; Cercignani 2000; Struchtrup 2005; Sone 2007; Torrilhon 2016). The classical continuum description based on the Euler or Navier–Stokes–Fourier (NSF) equations is valid only in regimes for which  $Kn \lesssim 0.001$ , this is referred to as the hydrodynamic regime. There are, of course, computational atomistic techniques, such as molecular dynamics (MD) simulations, which are capable of modelling phase transition at nanoscales. However, owing to computational time and memory limitations, it is impractical to use them for multiscale processes, which span a wide range of time and length scales.

The behaviour of a dilute vapour phase can readily be described by the Boltzmann equation, which is an evolution equation for the (velocity) distribution function of vapour molecules (Bird 1994; Cercignani 2000). The Boltzmann equation offers the complete mesoscopic description of the vapour for all ranges of  $Kn$ , however, the exact analytical solution of the Boltzmann equation is intractable in a general case, whereas its numerical solutions are computationally very expensive. Grad, in his seminal work (Grad 1949*a,b*), proposed an asymptotic solution procedure for the Boltzmann equation through the method of moments. A variety of other extended fluid-dynamics equations, aiming to describe processes under rarefied conditions, have been developed, see e.g. Eu (1992), Müller & Ruggeri (1998), Kremer (2010), Struchtrup (2005), Chakraborty & Durst (2007), Dongari, Chakraborty & Durst (2010), Myong (2014) and Torrilhon (2016). These models close the gap between classical fluid dynamics and kinetic theory; that is, they aim at a good description in the transition regime ( $0.001 \lesssim Kn \lesssim 1$ ).

The classical phase-transition models, found in the literature, assume that the temperature and the velocity tangential to the interface are continuous across it. However, it is now well established, both experimentally and theoretically (McGaughey & Ward 2002; Bond & Struchtrup 2004; Rana, Lockerby & Sprittles 2019), that such assumptions are invalid at a nano-confined liquid–vapour interface. For such small length scales, the Knudsen number lies in the transition regime (or beyond) and a difference in velocity and temperature jump are observed across the interface, thus, it is important to employ models capable of describing strong non-equilibrium effects that occur at high Knudsen numbers. In Rana *et al.* (2019), the lifetime of an evaporating nanodroplet was studied. The study revealed that, when the drop size is large (larger than a micrometre), the square of its diameter decreases in proportion to time, this is known as the  $d^2$ -law. However, as the diameter approaches sub-micrometre and nanoscales, a crossover to a new behaviour is observed, with the diameter now reducing in proportion to time (following a ‘ $d$ -law’). By taking into account the temperature discontinuity at the liquid–vapour interface, the drop’s lifetime was predicted correctly.

Notably, a full theory on boundary conditions is still missing for these nonlinear extended fluid-dynamics equations, for which the notion of solvability and stability is more intricate. The approach suggested by Grad (1958) and recently explored by researchers (Gu & Emerson 2007; Torrilhon & Struchtrup 2008; Gu & Emerson 2009; Struchtrup *et al.* 2017; Rana, Lockerby & Sprittles 2018*b*), violates Onsager symmetry conditions (Rana & Struchtrup 2016; Beckmann *et al.* 2018; Sarna & Torrilhon 2018), leading to instabilities which influence the convergence of numerical schemes and prevent the convergence of moments (Torrilhon & Sarna 2017; Zinner & Öttinger 2019).

The second law of thermodynamics (entropy inequality) plays an important role in finding constitutive relations in the bulk (de Groot & Mazur 1962; Gyarmati 1970; Harten 1983; Lebon, Jou & Casas-Vázquez 2008), in designing numerical schemes (Tadmor & Zhong 2006; Kumar & Mishra 2012; Chandrashekar 2013), as well as in developing physically admissible boundary conditions (Bond & Struchtrup 2004; Struchtrup & Torrilhon 2007; Kjelstrup & Bedeaux 2008; Rana & Struchtrup 2016; Schweizer, Öttinger & Savin 2016; Rana, Gupta & Struchtrup 2018*a*; Beckmann *et al.* 2018; Sarna & Torrilhon 2018). For the latter, one determines the entropy generation at the boundary and finds the boundary conditions as phenomenological laws that guarantee positivity of the entropy generation at the boundary. For example, in Struchtrup & Torrilhon (2007), Rana & Struchtrup (2016), Sarna & Torrilhon (2018) and Beckmann *et al.* (2018) the linearised second law (taking a quadratic entropy) was employed to determine boundary conditions for the linearised version of the moment equations. The resulting phenomenological boundary conditions were thermodynamically consistent for all processes and complied with the Onsager reciprocity relations (Onsager 1931).

Over the last few years, an impressive body of research work has been devoted to the development of constitutive theories whose closed conservation laws guarantee the second law (Öttinger 2010; Struchtrup & Torrilhon 2010; Torrilhon 2012; Liu *et al.* 2013; Paolucci & Paolucci 2018). The Burnett equations, which are obtained perturbatively from the kinetic theory, are unstable (Bobylev 2006) and owing to the lack of any coherent second law these equations lead to physically inadmissible solutions (Struchtrup & Nadler 2020). The Burnett equations are unstable owing to the lack of a proper entropy inequality. On the other hand, the moment equations (Grad 13-moment equations, regularised 13-moment equations, etc.) are accompanied by proper entropy inequalities, and are stable, but only in the linear cases (Struchtrup & Torrilhon 2007; Rana & Struchtrup 2016; Torrilhon & Sarna 2017). In Rana *et al.* (2018*a*), the coupled constitutive relations (CCRs) were obtained, as an enhancement to the NSF equations, by considering a correction term to the non-convective entropy flux (in addition to the classic entropy flux, i.e. heat-flux and thermodynamic temperature). As a result, the CCRs add several second-order terms to the NSF equations, in the bulk and in the boundary conditions, capturing important rarefaction effects in moderately rarefied conditions, such as the Knudsen minimum, and non-Fourier heat transfer, which cannot be described by classical hydrodynamics (Rana *et al.* 2018*a*).

Throughout this paper, we are going to utilise the CCR theory, thereby some comments about these equations are in order. The CCR theory originates from the arguments of irreversible thermodynamics. In CCR theory, additional terms appear in the constitutive relations of the NSF equations, where the coupling between constitutive relations for the heat-flux vector and stress tensor is introduced via a coupling coefficient ( $\alpha_0$ ). For  $\alpha_0 = 0$ , the coupling vanishes and one obtains the classical NSF equations. In addition, for the flow conditions considered in the paper (steady-state and linearised equations), the CCR system (conservation laws plus CCR) reduces to the linearised Grad 13-moment equations (Grad-13) for  $\alpha_0 = 2/5$ ; a value obtained for Maxwell molecule

(MM) gases (Struchtrup 2005). Thus, under suitable assumptions, this paper provides a unified framework for the NSF equations, Grad-13 and the CCR system. More precisely, we explore the method of fundamental solutions (MFS) for the CCR system (hence, NSF, Grad-13) that can be useful for constructing solutions over a wide range of free-stream profiles and complex geometries.

The MFS (Kupradze & Aleksidze 1964) is a mesh-free numerical technique for solving partial differential equations based on using the fundamental solutions (Green's functions). The main advantage that the MFS has over the more classical numerical methods, such as the finite-difference method and the finite-element method, is that its solution procedure does not require discretisation of the interior of the computational domain, thus a significant amount of computational effort and time is saved. Furthermore, the MFS does not require (the very computationally expensive) three-dimensional mesh generation. As a result, the MFS is ideally suited for the problems involving moving interfaces and phase-change processes. The first steps towards utilising MFS for rarefied gas flows were taken by Lockerby & Collyer (2016), who derived Green's functions for the Grad-13 system and utilised them to solve some canonical problems. The present study further develops the MFS-based framework (MFS-CCR) for phase-transition boundary-value problems, which, as we show later, involves the derivation of new Green's functions, generated by a singular mass source/sink term. In this paper, a set of temperature-jump and velocity-slip boundary conditions for a liquid-vapour interface will be derived for the linearised CCR system and implemented within the framework of MFS. However, it should be noted that the developed MFS methodology in this paper can also be applied to other type of liquid-vapour interface boundary conditions, such as the classical Schrage law (Schrage 1953), statistical rate theory (Ward & Fang 1999) and phenomenological approach based on Hertz-Knudsen-Schrage relation (Liang, Biben & Koblinski 2017). We do not address these boundary conditions in this paper, instead we leave this for a future investigation.

The remainder of this paper is organised as follows. In § 2, we introduce the linearised and dimensionless CCR model. In § 3, the derivation of Green's functions for the CCR model is presented, followed by the derivation of thermodynamically consistent boundary conditions at the phase interface in § 4. A brief summary of the MFS and implementation is given in § 5. In § 6.1 the numerical scheme is applied to evaporation from a spherical droplet and low-speed gas flow around a sphere (for which the analytical solutions exist) in order to validate our numerical scheme. To illustrate the utility of fundamental solutions for complex geometries, in §§ 6.2, 6.3 and 6.4 we solve the motion of two spherical non-evaporating droplets with different orientations, evaporation of two interacting droplets and evaporation of a deformed droplet, respectively. Concluding remarks are made in § 8.

## 2. The linearised NSF, Grad-13 and CCR systems

In this paper we only consider flow conditions where the deviations from a constant equilibrium state, given by a constant reference density  $\hat{\rho}_0$ , a constant reference temperature  $\hat{T}_0$  and all other fields zero, are small. Thereby, the governing equations can be linearised with respect to the reference state. The governing equations are put into dimensionless form by introducing

$$\mathbf{r} = \frac{\hat{\mathbf{r}}}{\hat{\ell}}, \quad \rho = \frac{\hat{\rho} - \hat{\rho}_0}{\hat{\rho}_0} \quad \text{and} \quad T = \frac{\hat{T} - \hat{T}_0}{\hat{T}_0}, \quad (2.1a-c)$$

where  $\mathbf{r}$  is the position vector in Cartesian coordinates,  $\hat{\ell}$  is the reference length scale and  $\rho$  and  $T$  are the dimensionless perturbations in the density and temperature from their reference values, respectively; hats denote dimensional quantities. The dimensionless velocity vector  $\mathbf{v}$ , the stress tensor  $\mathbf{\Pi}$  and the heat-flux vector  $\mathbf{q}$  are

$$\mathbf{v} = \frac{\hat{\mathbf{v}}}{\sqrt{\hat{R}\hat{T}_0}}, \quad \mathbf{\Pi} = \frac{\hat{\mathbf{\Pi}}}{\hat{\rho}_0\hat{R}\hat{T}_0} \quad \text{and} \quad \mathbf{q} = \frac{\hat{\mathbf{q}}}{\hat{\rho}_0(\hat{R}\hat{T}_0)^{3/2}}, \quad (2.2a-c)$$

where  $\hat{R}$  is the gas constant. The perturbation in pressure  $p$  is given by a linearised equation of state

$$p = \frac{\hat{\rho}\hat{R}\hat{T}}{\hat{\rho}_0\hat{R}\hat{T}_0} - 1 = (1 + \rho)(1 + \theta) - 1 \approx \rho + \theta, \quad (2.3)$$

where the last equation assumes small perturbations  $\rho$  and  $\theta$ , hence  $\rho\theta$  is assumed to be negligible in comparison to  $\rho + \theta$ .

Accordingly, dimensionless and steady-state (linearised) conservation laws for mass, momentum and energy read

$$\nabla \cdot \mathbf{v} = 0, \quad \nabla p + \nabla \cdot \mathbf{\Pi} = 0 \quad \text{and} \quad \nabla \cdot \mathbf{q} = 0. \quad (2.4a-c)$$

It should be noted that conservation laws (2.4a-c) contain the stress tensor and heat-flux vector as unknowns, hence constitutive equations are required for these quantities. If the CCR closure is adopted, the (linearised) constitutive relations for  $\mathbf{\Pi}$  and  $\mathbf{q}$  read (Rana *et al.* 2018a)

$$\mathbf{\Pi} = -2Kn\langle\nabla\mathbf{v}\rangle - 2\alpha_0Kn\langle\nabla\mathbf{q}\rangle \quad \text{and} \quad \mathbf{q} = -\frac{c_pKn}{Pr}(\nabla T + \alpha_0\nabla \cdot \mathbf{\Pi}), \quad (2.5a,b)$$

where  $c_p = 5/2$  ( $=\hat{c}_p/\hat{R}$ ) is the specific heat for mono-atomic gases,  $Pr$  is the Prandtl number and the Knudsen number  $Kn = \hat{\mu}_0/(\hat{\rho}_0\sqrt{\hat{R}\hat{T}_0}\hat{\ell})$ , where  $\hat{\mu}_0$  is the viscosity of the gas at the reference state. Furthermore, the chevrons in (2.5a,b) denote the traceless and symmetrical component of the tensor, i.e.

$$\langle\nabla\mathbf{v}\rangle = \frac{1}{2}(\nabla\mathbf{v} + \nabla\mathbf{v}^T) - \frac{1}{3}(\nabla \cdot \mathbf{v})\mathbf{I}, \quad (2.6)$$

where  $\mathbf{I}$  is the identity matrix.

It is because the constitutive relations (2.5a,b) for the fluxes  $\mathbf{\Pi}$  and  $\mathbf{q}$  are coupled (in contrast to NSF) that they are given the initialism CCRs. The benefit of the CCR model compared with extended moment equations (Grad-13 equations, for instance) is that it retains full thermodynamic structure without any restriction (Rana *et al.* 2018a).

In the above equations the phenomenological coefficient  $\alpha_0$  appears, which is chosen such that the CCR model agrees with the Burnett coefficients (in the sense of the Chapman–Enskog expansion of the Boltzmann equation). The NSF equations are obtained when  $\alpha_0 = 0$ . The value of  $\alpha_0$  for the MM gases is  $2/5$ , for other power potentials it can be computed from the relation  $\alpha_0 = Pr\omega_3/5$ , where  $\omega_3$  is the Burnett coefficient (Struchtrup 2005; Rana *et al.* 2018a).

It is important to note here that, in steady state, the linearised CCR model reduces to the linearised Grad-13 moment equations for  $\alpha_0 = 2/5$  (i.e. for MM gases). Hence, using the naming convention of Lockerby & Collyer (2016), Claydon *et al.* (2017), the solution of the CCR equations (2.4a-c) and (2.5a,b) will still be referred to as the generalised Gradlet.

### 3. Green’s functions: the Gradlet, thermal Gradlet and sourcelet

In this section, we write the fundamental solutions (Green’s functions) for the CCR system (2.4a–c) and (2.5a,b) that will be used further in constructing the new solutions for complex geometries and phase-change problems.

#### 3.1. The Gradlet and thermal Gradlet

The fundamental solutions sought here correspond to the steady-state response of the vapour with regard to a point body force  $\mathbf{f}$  and a heat source of strength  $g$ , acting at the singularity point at the origin ( $\mathbf{r}^s = 0$ ), i.e. the Green’s functions associated with the following equations:

$$\nabla \cdot \mathbf{v} = 0, \quad \nabla p + \nabla \cdot \boldsymbol{\Pi} = Kn\mathbf{f}\delta(\mathbf{r}) \quad \text{and} \quad \nabla \cdot \mathbf{q} = Kng\delta(\mathbf{r}), \quad (3.1a-c)$$

where  $\delta(\mathbf{r})$  is the three-dimensional Dirac delta function. The solutions to (3.1a–c) along with (2.5a,b) are obtained via a Fourier transformation. The velocity  $\mathbf{v}^{(Gr)}$ , pressure  $p^{(Gr)}$  and stress tensor  $\boldsymbol{\Pi}^{(Gr)}$ , at any point  $\mathbf{r}$ , are found as

$$\mathbf{v}^{(Gr)}(\mathbf{r}) = \frac{1}{8\pi}\mathbf{J}(\mathbf{r}) \cdot \mathbf{f} + \frac{3\alpha_0^2 c_p Kn^2}{4\pi Pr}\mathbf{K}(\mathbf{r}) \cdot \mathbf{f}, \quad (3.2a)$$

$$p^{(Gr)}(\mathbf{r}) = \frac{Kn}{4\pi} \frac{\mathbf{f} \cdot \mathbf{r}}{|\mathbf{r}|^3}, \quad (3.2b)$$

$$\boldsymbol{\Pi}^{(Gr)}(\mathbf{r}) = \frac{3Kn}{4\pi} (\mathbf{f} \cdot \mathbf{r} + 2\alpha_0 Kng) \mathbf{K}(\mathbf{r}). \quad (3.2c)$$

Here, we have introduced the abbreviations

$$\mathbf{J}(\mathbf{r}) = \frac{\mathbf{r}\mathbf{r}}{|\mathbf{r}|^3} + \frac{\mathbf{I}}{|\mathbf{r}|} \quad \text{and} \quad \mathbf{K}(\mathbf{r}) = \frac{\mathbf{r}\mathbf{r}}{|\mathbf{r}|^5} - \frac{1}{3} \frac{\mathbf{I}}{|\mathbf{r}|^3} \quad (3.3a,b)$$

to denote the Oseen–Burger tensor and the third decaying harmonic tensor (Lamb 1945), respectively. The temperature  $T^{(Gr)}$  and heat flux  $\mathbf{q}^{(Gr)}$  are obtained as

$$T^{(Gr)}(\mathbf{r}) = \frac{Pr}{4\pi c_p} \frac{g}{|\mathbf{r}|}, \quad (3.4a)$$

$$\mathbf{q}^{(Gr)}(\mathbf{r}) = \frac{Kn}{4\pi} \frac{g}{|\mathbf{r}|^3} \mathbf{r} - \frac{3\alpha_0 c_p Kn^2}{4\pi Pr} \mathbf{K}(\mathbf{r}) \cdot \mathbf{f}. \quad (3.4b)$$

Here, it is assumed that all the field variables are measured relative to their equilibrium values at infinity, hence all field variables vanish as  $|\mathbf{r}| \rightarrow \infty$ .

One can easily verify that, for  $\alpha_0 = 0$ , the fundamental solutions (3.2) and (3.4) reduce to the solution of Stokes (Stokeslet) and the heat equation (thermal Stokeslet), which is available in the works of Oseen and Burger (Lamb 1945) and the recent work of Lockerby & Collyer (2016). Moreover, for  $\alpha_0 = 2/5$ , (3.2)–(3.4) reduce to the Grad-13 moment equations, the Gradlet and the thermal Gradlet, obtained by Lockerby & Collyer (2016). Thus, one can also think of (3.2)–(3.4) as the solution of 13-moment equations (steady-state and linearised) with general power potentials in the collision operator for the Boltzmann equation.



3.2. The sourcelet

The linearity of (2.4a–c) and (2.5a,b) allows one to obtain a class of singularity solutions that are readily applicable to various type of boundary-value problems. Note that the fundamental solutions (Gradlet and thermal Gradlet) obtained in the previous section create no mass flux. Owing to Gauss’ theorem, one may draw any boundary enclosing the Stokeslet/Gradlet, and find that there can be no mass flux across it ( $\nabla \cdot \mathbf{v} = 0$  everywhere). Therefore, it follows that, to capture phase-change events (and here we are particularly interested in the liquid–vapour interface) an additional fundamental solution is required, one that produces a source of mass. Hence, we consider the solution of the following equations:

$$\nabla \cdot \mathbf{v} = h\delta(\mathbf{r}), \quad \nabla p + \nabla \cdot \mathbf{\Pi} = 0, \quad \text{and} \quad \nabla \cdot \mathbf{q} = 0, \quad (3.5a-c)$$

where  $h$  is the strength of the mass source. Again, the fundamental solutions of (3.5a–c) and (2.5a,b) are derived via Fourier transform (see Appendix A for detailed derivation), yielding

$$\mathbf{v}^{(S)}(\mathbf{r}) = \frac{h}{4\pi} \frac{\mathbf{r}}{|\mathbf{r}|^3}, \quad (3.6a)$$

$$\mathbf{\Pi}^{(S)}(\mathbf{r}) = \frac{3Kn h}{2\pi} \mathbf{K}(\mathbf{r}), \quad (3.6b)$$

$$p^{(S)}(\mathbf{r}) = T^{(S)}(\mathbf{r}) = 0 \quad \text{and} \quad \mathbf{q}^{(S)}(\mathbf{r}) = 0. \quad (3.6c)$$

As such, the pressure, temperature and heat flux vanish for this case.

3.3. Equations collected

Combining the Gradlet, thermal Gradlet (3.2)–(3.4) and sourcelet (3.6), the flow fields induced by the generalised Gradlet (a point mass source, point force and point heat source) are

$$\mathbf{v}(\mathbf{r}) = \frac{1}{8\pi} \mathbf{J}(\mathbf{r}) \cdot \mathbf{f} + \frac{3\alpha_0^2 c_p Kn^2}{4\pi Pr} \mathbf{K}(\mathbf{r}) \cdot \mathbf{f} + \frac{h}{4\pi} \frac{\mathbf{r}}{|\mathbf{r}|^3}, \quad (3.7a)$$

$$p(\mathbf{r}) = \frac{Kn \mathbf{f} \cdot \mathbf{r}}{4\pi |\mathbf{r}|^3}, \quad (3.7b)$$

$$\mathbf{\Pi}(\mathbf{r}) = \frac{3Kn}{4\pi} (\mathbf{f} \cdot \mathbf{r} + 2\alpha_0 Kng + 2h) \mathbf{K}(\mathbf{r}) \quad (3.7c)$$

and

$$T(\mathbf{r}) = \frac{Pr}{4\pi c_p} \frac{g}{|\mathbf{r}|}, \quad (3.8a)$$

$$\mathbf{q}(\mathbf{r}) = \frac{Kn}{4\pi} \frac{g}{|\mathbf{r}|^3} \mathbf{r} - \frac{3\alpha_0 c_p Kn^2}{4\pi Pr} \mathbf{K}(\mathbf{r}) \cdot \mathbf{f}. \quad (3.8b)$$

These solutions need to be supplemented with appropriate boundary conditions, which are formulated in the next section.

#### 4. Liquid–vapour interface boundary conditions

In this section, we derive the phase-interface boundary conditions for the CCR system within the framework of irreversible thermodynamics (Kjelstrup & Bedeaux 2008). In order to establish (thermodynamically consistent) boundary conditions at the phase interface, one determines the entropy generation at the interface, and finds the boundary conditions as phenomenological laws that guarantee positivity of the entropy generation rate. For the linearised CCR equations, the entropy generation rate at the interface is (Beckmann *et al.* 2018; Rana *et al.* 2018a)

$$\Sigma_{surface} = -(\mathbf{v} - \mathbf{v}^l) \cdot \mathbf{n} [p - p_{sat} + (\mathbf{n} \cdot \mathbf{\Pi} \cdot \mathbf{n})] - \mathbf{q} \cdot \mathbf{n} [T - T^l + \alpha_0 (\mathbf{n} \cdot \mathbf{\Pi} \cdot \mathbf{n})] - \sum_{i=1}^2 (\mathbf{t}^{(i)} \cdot \mathbf{\Pi} \cdot \mathbf{n}) [\mathbf{t}^{(i)} \cdot (\mathbf{v} - \mathbf{v}^l) + \alpha_0 \mathbf{t}^{(i)} \cdot \mathbf{q}] \geq 0, \tag{4.1}$$

where  $\mathbf{n}$  is a unit normal pointing from a boundary point into the gas and  $\{\mathbf{t}^{(i)}\}_{i=1,2}$  are orthonormal tangent vectors to the boundary. Here,  $\mathbf{v}^l$  denotes the velocity of the interface,  $T^l$  denotes the temperature of the liquid at the interface and  $p_{sat}(T^l)$  is the saturation pressure.

The positivity of entropy generation rate  $\Sigma_{surface}$  is ensured by adopting the following boundary equations

$$(\mathbf{v} - \mathbf{v}^l) \cdot \mathbf{n} = -\eta_{11} (p - p_{sat} + \mathbf{n} \cdot \mathbf{\Pi} \cdot \mathbf{n}) + \eta_{12} (T - T^l + \alpha_0 \mathbf{n} \cdot \mathbf{\Pi} \cdot \mathbf{n}), \tag{4.2a}$$

$$\mathbf{q} \cdot \mathbf{n} = \eta_{12} (p - p_{sat} + \mathbf{n} \cdot \mathbf{\Pi} \cdot \mathbf{n}) - (\eta_{22} + 2\tau_0) (T - T^l + \alpha_0 \mathbf{n} \cdot \mathbf{\Pi} \cdot \mathbf{n}) \tag{4.2b}$$

and

$$\mathbf{t}^{(1)} \cdot \mathbf{\Pi} \cdot \mathbf{n} = -\zeta (\mathbf{v} - \mathbf{v}^l + \alpha_0 \mathbf{q}) \cdot \mathbf{t}^{(1)}, \tag{4.3a}$$

$$\mathbf{t}^{(2)} \cdot \mathbf{\Pi} \cdot \mathbf{n} = -\zeta (\mathbf{v} - \mathbf{v}^l + \alpha_0 \mathbf{q}) \cdot \mathbf{t}^{(2)}. \tag{4.3b}$$

Through boundary conditions (4.2), the evaporative mass and heat flux are governed by the difference between pressure and saturation pressure and temperature difference across the interface. Furthermore, the boundary conditions (4.3a) and (4.3b) relate the shear stress to the tangential velocity slip and thermal transpiration, a flow induced by a tangential heat flux, which is a second-order effect (Hadjiconstantinou 2003; Sone 2007; Cercignani & Lorenzani 2010). The boundary conditions (4.2) and (4.3) are an extension to the classical Hertz–Knudsen–Schrage law for evaporation (Schrage 1953), taking into account the temperature jump, velocity slip and some second-order effects.

In boundary conditions (4.2),  $\eta_{ij}$ 's are Onsager resistivity coefficients, which are obtained from the asymptotic ( $Kn \rightarrow 0$ ) kinetic theory (Sone 2007), as (see Appendix B for details)

$$\eta_{11} = 0.9134 \sqrt{\frac{2}{\pi}} \frac{\vartheta}{2 - \vartheta}, \quad \eta_{12} = 0.3915 \sqrt{\frac{2}{\pi}} \frac{\vartheta}{2 - \vartheta}, \quad \text{and} \quad \eta_{22} = 0.1678 \sqrt{\frac{2}{\pi}} \frac{\vartheta}{2 - \vartheta}. \tag{4.4a-c}$$

These coefficients were obtained assuming that the evaporation/condensation coefficient  $\vartheta$  is independent of the impact energy of molecules and that all vapour molecules that are not condensing are thermalised, i.e. the accommodation coefficient,  $\chi = 1$ .



The temperature-jump coefficient  $\tau_0 = 0.8503\sqrt{2/\pi}$  and velocity-slip coefficient  $\zeta = 0.8798\sqrt{2/\pi}$ . Throughout this paper, we shall take  $\vartheta = 0$  for the canonical boundaries and  $\vartheta = 1$  (a value largely accepted in literature) for the phase-change boundaries.

Although in the development of our MFS approach, we use (4.2) and (4.3) as the boundary conditions, this methodology is in principle capable of accommodating other type of phase-interface boundary conditions, such as statistical-rate theory (Ward & Fang 1999) and phenomenological approach based on Hertz–Knudsen–Schrage relation (Liang *et al.* 2017). We do not address these boundary conditions in this paper, but should be worthy of future investigation.

In the following sections, we introduce, and use, the MFS for CCR, i.e. CCR–MFS, which is computationally economic, and shows that it provides reliable solutions of the CCR and NSF equations in good agreement to the known closed-form analytical results.

### 5. MFS for the CCR equations (CCR–MFS)

Let us consider  $N_c$  collocation points on the boundary at  $\{\mathbf{r}^{c(j)}\}_{j=1}^{N_c}$ , whereas  $N_s$  singularity points are located outside the computational domain (i.e. inside the solid/liquid body) with position vectors  $\{\mathbf{r}^{s(j)}\}_{j=1}^{N_s}$ , see figure 1. The flow-field variables are given by a superposition of the Gradlets, thermal Gradlets and sourcelets, formulated in (3.7) and (3.8), as

$$\mathbf{v}^{(i)(Gr)} = \sum_{j=1}^{N_s} \frac{1}{8\pi} \mathbf{J}(\mathbf{r}^{(ij)}) \cdot \mathbf{f}^{(j)} + \frac{3\alpha_0^2 c_p Kn^2}{4\pi Pr} \mathbf{K}(\mathbf{r}^{(ij)}) \cdot \mathbf{f}^{(j)}, \quad (5.1a)$$

$$\mathbf{v}^{(i)(S)} = \sum_{j=1}^{N_s} \frac{h^{(j)}}{4\pi} \frac{\mathbf{r}^{(ij)}}{|\mathbf{r}^{(ij)}|^3}, \quad (5.1b)$$

$$\mathbf{v}^{(i)} = \mathbf{v}^{(i)(Gr)} + \mathbf{v}^{(i)(S)}, \quad (5.1c)$$

$$p^{(i)} = \sum_{j=1}^{N_s} \frac{Kn \mathbf{f}^{(j)} \cdot \mathbf{r}^{(ij)}}{4\pi |\mathbf{r}^{(ij)}|^3}, \quad (5.1d)$$

$$\Pi^{(i)} = \sum_{j=1}^{N_s} \frac{3Kn}{4\pi} \left( \mathbf{f}^{(j)} \cdot \mathbf{r}^{(ij)} + 2\alpha_0 Kn g^{(j)} + 2h^{(j)} \right) \mathbf{K}(\mathbf{r}^{(ij)}), \quad (5.1e)$$

and

$$T^{(i)} = \sum_{j=1}^{N_s} \frac{Pr}{4\pi c_p} \frac{g^{(j)}}{|\mathbf{r}^{(ij)}|}, \quad (5.2a)$$

$$\mathbf{q}^{(i)} = \sum_{j=1}^{N_s} \frac{Kn}{4\pi} \frac{g^{(j)} \mathbf{r}^{(ij)}}{|\mathbf{r}^{(ij)}|^3} - \frac{3\alpha_0 c_p Kn^2}{4\pi Pr} \mathbf{K}(\mathbf{r}^{(ij)}) \cdot \mathbf{f}^{(j)} \quad (5.2b)$$

are fundamental solutions for the CCR equations. Here,  $\mathbf{r}^{(ij)} = \mathbf{r}^{c(i)} - \mathbf{r}^{s(j)}$  are the displacement vectors from the  $j$ th singularity site to the  $i$ th collocation point.

There are a total of  $5 \times N^s$  unknowns in (5.1) and (5.2), five at each singularity site, which need to be specified via suitable boundary conditions. The four boundary conditions

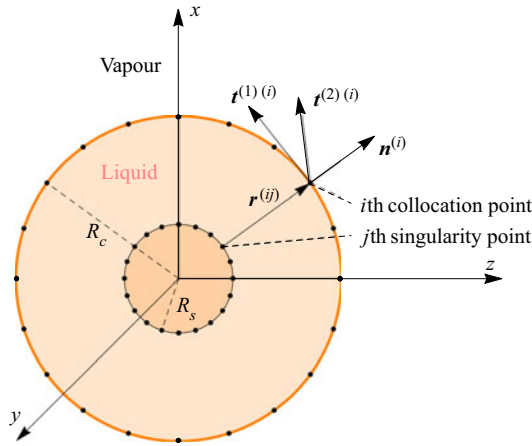


Figure 1. Schematic representation of the collocation and singularity points layout:  $\mathbf{n}^{(i)}$ ,  $\mathbf{t}^{(1)(i)}$  and  $\mathbf{t}^{(2)(i)}$  represent the unit normal and both the tangential vectors, respectively, at the  $i$ th collocation point.

in (4.2) and (4.3) need to be satisfied at every collocation point. Hence, one additional boundary condition is required (at each collocation point). We use the following boundary conditions:

$$\mathbf{v}^{(i)(S)} \cdot \mathbf{n}^{(i)} = -\eta_{11} \left( p^{(i)} - p_{sat}^{(i)} + \mathbf{n}^{(i)} \cdot \mathbf{\Pi}^{(i)} \cdot \mathbf{n}^{(i)} \right) + \eta_{12} \left( T^{(i)} - T^{(i)I} + \alpha_0 \mathbf{n}^{(i)} \cdot \mathbf{\Pi}^{(i)} \cdot \mathbf{n}^{(i)} \right), \tag{5.3a}$$

$$\left( \mathbf{v}^{(i)(Gr)} - \mathbf{v}^{(i)I} \right) \cdot \mathbf{n}^{(i)} = 0. \tag{5.3b}$$

Notably, we have split the boundary condition (4.2a) into two components, (5.3a) and (5.3b). Clearly, these two boundary conditions are sufficient for condition (4.2a) to hold. The boundary conditions for the normal heat flux (4.2b) and shear stress (4.3) read

$$\mathbf{q}^{(i)} \cdot \mathbf{n}^{(i)} = \eta_{12} \left( p^{(i)} - p_{sat}^{(i)} + \mathbf{n}^{(i)} \cdot \mathbf{\Pi}^{(i)} \cdot \mathbf{n}^{(i)} \right) - (\eta_{22} + 2\tau_0) \left( T^{(i)} - T^{(i)I} + \alpha_0 \mathbf{n}^{(i)} \cdot \mathbf{\Pi}^{(i)} \cdot \mathbf{n}^{(i)} \right), \tag{5.4a}$$

$$\mathbf{t}^{(1)(i)} \cdot \mathbf{\Pi}^{(i)} \cdot \mathbf{n}^{(i)} = -\zeta \left( \mathbf{v}^{(i)} - \mathbf{v}^{(i)I} + \alpha_0 \mathbf{q}^{(i)} \right) \cdot \mathbf{t}^{(1)(i)}, \tag{5.4b}$$

$$\mathbf{t}^{(2)(i)} \cdot \mathbf{\Pi}^{(i)} \cdot \mathbf{n}^{(i)} = -\zeta \left( \mathbf{v}^{(i)} - \mathbf{v}^{(i)I} + \alpha_0 \mathbf{q}^{(i)} \right) \cdot \mathbf{t}^{(2)(i)}. \tag{5.4c}$$

For convenience, we write the set of equations (5.3) and (5.4) in matrix form

$$\sum_{j=1}^{N^s} \mathcal{L}^{ij} \mathbf{u}^{(j)} = \mathbf{b}^{(i)}, \tag{5.5}$$

where  $\mathbf{u}^{(j)}$  is the vector containing the five degrees of freedom at each singularity point, i.e.

$$\mathbf{u}^{(j)} = \left\{ g^{(j)}, f_1^{(j)}, f_2^{(j)}, f_3^{(j)}, h^{(j)} \right\}, \tag{5.6}$$

where  $\mathcal{L}^{ij}$  is a  $5 \times 5$  coefficient matrix, and  $\mathbf{b}^{(i)}$  is a  $5 \times 1$  vector, which can be readily extracted using symbolic software, we used Mathematica<sup>®</sup> for this. The inhomogeneous part  $\{\mathbf{b}^{(i)}\}_{i=1}^{N^c}$  contains the properties of the interface, namely,  $T^{(i)I}$ ,  $p_{sat}^{(i)}$  and  $\mathbf{v}^{(i)I}$ . The  $5N^c \times 5N^s$  linear system (5.5) is solved for  $\{\mathbf{u}^{(i)}\}_{i=1}^{N^s}$  using an iterative quasi-minimal residual method (Freund & Nachtigal 1991). Moreover, the normal and the tangent vectors  $\{\mathbf{n}^{(j)}, \mathbf{t}^{(1)(j)}, \mathbf{t}^{(2)(j)}\}_{j=1}^{N^c}$  are obtained using Householder reflection formula for vector orthogonalisation (Lopes, Silva & Ambrósio 2013).

## 6. Results and discussion

The CCR–MFS method described in the previous section requires some numerical parameters to be specified, namely, the number of collocation ( $N^c$ ) and singularity ( $N^s$ ) points to take and the location of singularity points outside the computational domain. These parameters govern the overall efficiency of the numerical scheme, by striking a balance between numerical error and computational time. Throughout this study, we consider an equal number of collocation and singularity points, i.e.  $N^c = N^s$  and take  $\gamma \in (0, 1)$  as a geometry-dependent parameter, which governs how far the singularity points are from the boundary. For instance, for the spherical geometry shown in figure 1, we choose  $\gamma = R_s/R_c$ .

In order to validate our code and to establish the numerical accuracy of the CCR–MFS scheme, we validate our results for a case of an evaporating spherical droplet, the analytic solutions to this problems are readily available in Rana *et al.* (2018*b*) for the case of Grad-13 equations. In addition, in order to establish the accuracy of our models, we consider a slow flow around a sphere (evaporative and non-evaporative) for various values of Knudsen number and compare our solutions with results from kinetic theory.

### 6.1. Validation and verification of CCR–MFS

#### 6.1.1. Validation case: evaporation from a spherical droplet

First, we consider a liquid droplet of fixed radius with a given interface temperature  $T^I$  and the corresponding saturation pressure  $p_{sat}$ , immersed in its own vapour, see figure 2. The far-field conditions are given by  $T_\infty = 0$ ,  $p_\infty = 0$ , that is, we consider the far-field conditions and the droplet radius ( $R_0$ ) for non-dimensionalisation. Throughout this paper we do not consider dynamics within the droplets, surface tension, etc., see Rana *et al.* (2019).

Assuming the spherical symmetry of this problem, the analytic solutions for the radial velocity  $v_r$ , heat flux  $q_r$ , normal stress  $\Pi_{rr}$  and the temperature  $T$  are obtained from (2.4*a–c*) and (2.5*a,b*) as (Rana *et al.* 2018*b*)

$$v_r = \frac{c_1}{r^2}, \quad q_r = \frac{c_2}{r^2}, \quad \Pi_{rr} = \frac{4Kn(c_1 + \alpha_0 c_2)}{r^3}, \quad T = \frac{Pr}{c_p Kn} \frac{c_2}{r}, \quad \text{and} \quad p = 0. \tag{6.1a–e}$$

Here,  $r$  is the radial direction and  $c_1$  and  $c_2$  are constants of integration. Solutions (6.1*a–e*) can also be derived from the fundamental solutions (3.7*a*)–(3.7*c*), which are given in Appendix C.

The flow is driven by (i) a unit pressure difference while the temperature of the liquid is equal to the far-field temperature (i.e.  $p_{sat} = 1$  and  $T^I = T_\infty = 0$ ) or (ii) a unit temperature difference while the saturation pressure in the liquid is the same as the far-field pressure (i.e.  $p_{sat} = p_\infty = 0$  and  $T^I = 1$ ). In both cases, the constants of integration, namely,

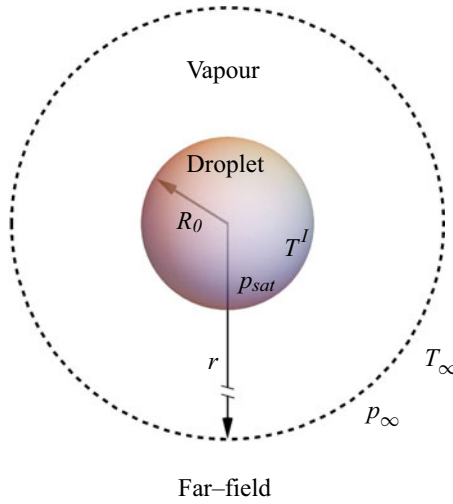


Figure 2. Schematic representation of a liquid droplet surrounded by its own vapour. The equations are made dimensionless with respect to the far-field conditions  $(T_\infty, p_\infty)$ . The temperature and the pressure deviations vanish as  $r \rightarrow \infty$ .

the mass flux ( $c_1$ ) and heat flux ( $c_2$ ), per unit area, are obtained from boundary conditions (4.2) at  $r = 1$ . For Grad-13 (i.e.  $\alpha_0 = 2/5$ ) these are obtained as

$$c_1^p = 0.220562 + \frac{0.0613424 + 0.0960246Kn}{0.138548 + Kn(0.716085 + Kn)}, \tag{6.2a}$$

$$c_2^p = c_1^\tau = -\frac{Kn(0.108868 + 0.551404Kn)}{0.138548 + Kn(0.716085 + Kn)}, \tag{6.2b}$$

$$c_2^\tau = \frac{0.152568Kn + Kn^2(0.924355 + 1.37851Kn)}{0.0406847 + Kn(0.348827 + Kn(1.00974 + Kn))}. \tag{6.2c}$$

Here, superscripts ‘ $p$ ’ and ‘ $\tau$ ’ denote the pressure-driven case ( $p_{sat} = 1$  and  $T^I = T_\infty = 0$ ) and temperature-driven case ( $p_{sat} = p_\infty = 0$  and  $T^I = 1$ ), respectively. The results of these two problems can be combined to evaluate the total evaporative mass and heat flux from the droplet (Rana *et al.* 2019). Owing to the microscopic reversibility of the evaporation and condensation processes the Onsager reciprocity relations hold, which give ( $c_2^p = c_1^\tau$ ) (Chernyak & Margilevskiy 1989; Rana *et al.* 2018b).

The mass and the heat flux predicted by the CCR–MFS method are obtained by integrating  $\mathbf{v}^{(Gr)}$  (5.1a), (5.1b) and  $\mathbf{q}^{(Gr)}$  (5.2b) over the droplet surface, i.e.

$$c_1^{(MFS)} = \frac{1}{4\pi} \int_0^\pi \int_0^{2\pi} \mathbf{v}^{(Gr)} \cdot \mathbf{n} \, d\varphi \, d\theta = \frac{1}{4\pi} \sum_{i=1}^{N^s} h^{(i)}, \tag{6.3}$$

$$c_2^{(MFS)} = \frac{1}{4\pi} \int_0^\pi \int_0^{2\pi} \mathbf{q}^{(Gr)} \cdot \mathbf{n} \, d\varphi \, d\theta = \frac{Kn}{4\pi} \sum_{i=1}^{N^s} g^{(i)}. \tag{6.4}$$

Let us first briefly consider the convergence characteristics of the CCR–MFS method. The configuration for the collocation and singularity points is shown in figure 1. We define

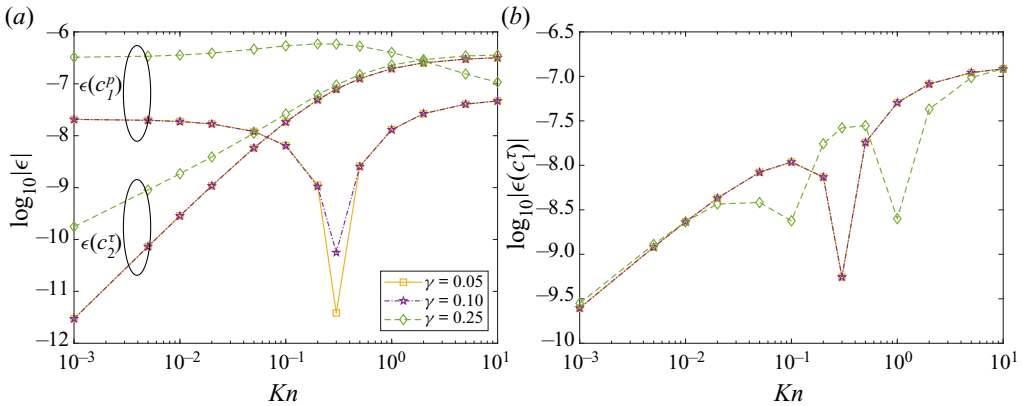


Figure 3. Log–log plot of errors against Knudsen number with three different singularity locations  $\gamma = R_s/R_c = 0.05, 0.1, 0.25$  and with  $N^c = N^s = 112$ : (a) error in  $c_1^p$  and  $c_2^\tau$  and (b) error in  $c_1^\tau$ .

errors  $\epsilon$  between the numerical prediction of  $c_1^p$ ,  $c_1^\tau$  and  $c_2^\tau$  to the analytical values (6.2) as

$$\epsilon(c_1^p) = c_1^{p(MFS)} - c_1^p, \quad \epsilon(c_2^\tau) = c_2^{\tau(MFS)} - c_2^\tau \quad \text{and} \quad \epsilon(c_1^\tau) = c_1^{\tau(MFS)} - c_1^\tau. \quad (6.5a-c)$$

Figure 3 shows the numerical errors of the MFS (with  $\alpha_0 = 2/5$ ) in  $c_1^p$ ,  $c_2^\tau$  (a) and  $c_1^\tau$  (b) for three different singularity site locations ( $\gamma = R_s/R_c = 0.05, 0.1, 0.25$ ) and various values of the Knudsen number. The result indicates very high accuracy with a moderate number of points ( $N^c = 112$ ). The best results are obtained when the singularity sites are farther away from the collocation nodes, i.e.  $\gamma$  is small. However, it leads to poorer conditioning of the equation system (5.5), which in turn results in larger least-square errors and computational time.

As Lockerby & Collyer (2016), numerical tests were also conducted by increasing the number of collocation points, as well as, by shifting the singularities sites (i.e. breaking the symmetry of the collocation and singularity points), the results were found to be satisfactory. Henceforth, the numerical simulations are performed with  $\gamma = 0.1$ , unless otherwise stated.

Figure 4 shows the variations in the mass- and heat-flux coefficients ( $c_1$  and  $c_2$ ) for a range of Knudsen numbers, the numerical parameters are included in the caption. In order to put the CCR models into perspective, we compare our predictions with different theories, namely, NSF ( $\alpha_0 = 0$ ), Grad-13 ( $\alpha_0 = 2/5$ ) and ( $\alpha_0 = 3/5$ ), against the results (symbols) from the linearised Boltzmann equations (LBEs) by Takata *et al.* (1998). The solutions of the NSF equations with classical boundary conditions, i.e. assuming the (linearised) Hertz–Knudsen–Schrage law for evaporation (Schrage 1953) and the continuity of temperature across the interface, are also included (thin green lines) in figure 4 for the comparison. These boundary conditions can be obtained from (4.2a) by taking  $\eta_{12} = 0$  and  $T = T^l$  instead of (4.2a), which are only valid for  $Kn \rightarrow 0$  (Sone 2007; Rana *et al.* 2018b).

For the pressure-driven case (cf. figure 4a) mass flux goes from liquid to vapour (i.e.  $c_1^p \geq 0$ ) and heat flows from vapour to liquid (i.e.  $c_2^\tau = c_1^\tau \leq 0$ ) because the enthalpy of phase change must be supplied to the droplet to keep its temperature constant. All models agree in the limit of  $Kn \rightarrow 0$  for the mass flux, the NSF equations with temperature-jump boundary conditions give better results over classical theories

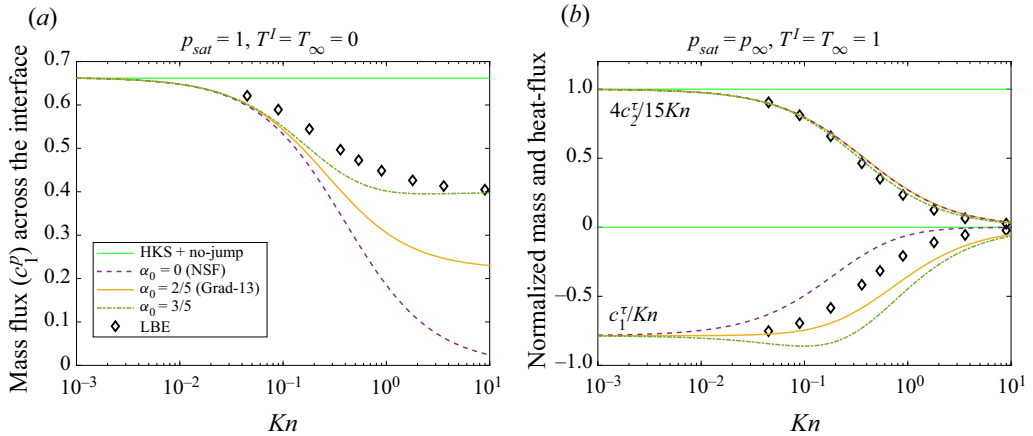


Figure 4. Mass- and heat-flux coefficients as a function of the Knudsen number: (a) mass flux ( $c_1^p$ ) in pressure-driven case and (b) normalised mass ( $c_1^\tau/Kn$ ) and heat flux ( $4c_2^\tau/15Kn$ ) coefficients in the temperature-driven case. The results obtained from MFS with different theories are compared. The symbols denoting the results from Takata *et al.* (1998) and (green) thin line representing the analytic results from classical boundary conditions. The number of collocation nodes used in each case are  $N^c = N^s = 112$  and  $\gamma = 0.1$ .

as the Knudsen number grows. Interestingly, the NSF equations with jump boundary conditions predicts a zero mass flux in the free-molecular regime, these results contradict kinetic-theory predictions. On the other hand, the Grad-13 theory gives a non-zero mass flux, but still predicts almost half of the mass flux of the LBE result. By performing an asymptotic expansion and matching the mass flux as  $Kn \rightarrow \infty$ , we find  $\alpha_0 = 3/5$  (a value extensively used in this study), with this model consequently providing the best agreement with the LBEs.

For the temperature-driven case (cf. figure 4b), Fourier’s law with a no-jump boundary condition gives heat flux  $c_2^\tau = 15Kn/4$ , while the cross effects, i.e. the heat flux owing to pressure difference or the mass flux owing to temperature difference, vanish. We have used this value to normalise the heat-flux computation in figure 4(b). All models, except the no-jump boundary conditions (thin green lines), match reasonably well with the LBE data, with  $\alpha_0 = 3/5$  giving a slight improvement over other models. However, the cross effects ( $c_1^\tau$ ) are not well captured by CCR theory, which requires resolution of the Knudsen layer, these are beyond the capabilities of the models considered in this paper, see Rana *et al.* (2018b) for a discussion on this.

### 6.1.2. Slow flow around a rigid sphere

Let us now consider the case of low-speed rarefied gas flow around a rigid ( $\vartheta = 0$ ) spherical stationary particle of radius  $R_0$ . The particle is assumed to be isothermal, that is, the solid-to-gas conductivity ratio is large, with  $T^I = 0$ , i.e. the far-field temperature and the temperature of the particle are same. The net force exerted on the sphere by gas is defined as

$$\mathbf{F}^{(Gr)} = \int_0^\pi \int_0^{2\pi} \left( p^{(Gr)} \mathbf{I} + \boldsymbol{\Pi}^{(Gr)} \right) \cdot \mathbf{n} \, d\varphi \, d\theta = Kn \sum_{i=1}^{N^s} \mathbf{f}^{(i)}. \quad (6.6)$$



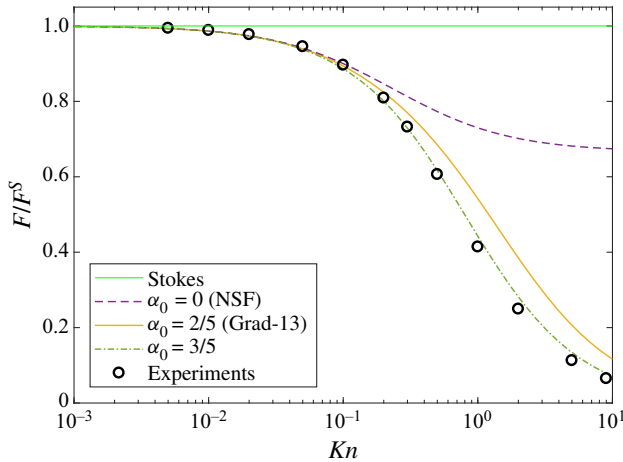


Figure 5. The normalised drag force computed from the CCR–MFS, with  $\alpha_0 = 0$  (NSF),  $\alpha_0 = 2/5$  (Grad-13) and  $\alpha_0 = 3/5$  against Knudsen number. The experimental data of Millikan (1923) (fitted by Allen & Raabe (1982)) is plotted (circles) for comparison. The results are normalized with Stokes’ drag (6.7).

The drag force is the projection of the net force (6.6) on to the streamwise direction. The Stokes formula for drag force (in the direction of flow) exerted by a spherical particle on the fluid flow has the form Lamb (1945)

$$F^S = -6\pi Kn u_\infty, \tag{6.7}$$

where  $u_\infty$  is the far-field velocity.

The Stokes formula is only valid for  $Kn \rightarrow 0$ , and requires corrections at finite Knudsen number. Figure 5 shows the normalised (with Stokes’ drag (6.7)) drag coefficient versus the Knudsen number. As expected, all theories agree in the small Knudsen limit. As the value of Knudsen number increases, the normalised drag decreases owing to increasing slip (which is not embedded in the Stokes formula). Notably, the normalised drag force reaches a finite value from the NSF equations with velocity-slip boundary conditions as  $Kn \rightarrow \infty$ , whereas the extended theories (CCR) predict a vanishing drag in this limit, an observation tantamount to experimental results. Nevertheless, between Grad-13 ( $\alpha_0 = 2/5$ ) and the CCR, with phenomenological coefficient  $\alpha_0 = 3/5$ , the latter gives the best quantitative agreement for values of the Knudsen number beyond unity (i.e. well beyond its apparent limits of applicability).

### 6.1.3. Slow flow around a spherical liquid droplet

In this section, we consider uniform flow (say, along the  $z$ -direction) of a saturated vapour over a spherical liquid droplet with a uniform temperature. The far-field temperature of the surrounding vapour is same as that of the droplet, i.e.  $T^I = T_\infty = 0$ ,  $p_{sat} = p_\infty = 0$  and  $\mathbf{v}_\infty = -\mathbf{v}^I = \{0, 0, u_\infty\}$ . We further assume that the droplet size remains fixed (quasi-steady-state assumption) and that deformation of the droplet is negligible, that is, the capillary number is very small.

Figure 6 shows the normalised drag force on a liquid droplet versus Knudsen number, while allowing phase-change at the interface. This problem has been considered by Sone *et al.* (1994) from the LBE, and is clearly important from an engineering point of view. Owing to the motion of the vapour phase, evaporation and condensation take place on the surface of the droplet, thereby slightly reducing the drag on the sphere, cf. figures 5 and 6.

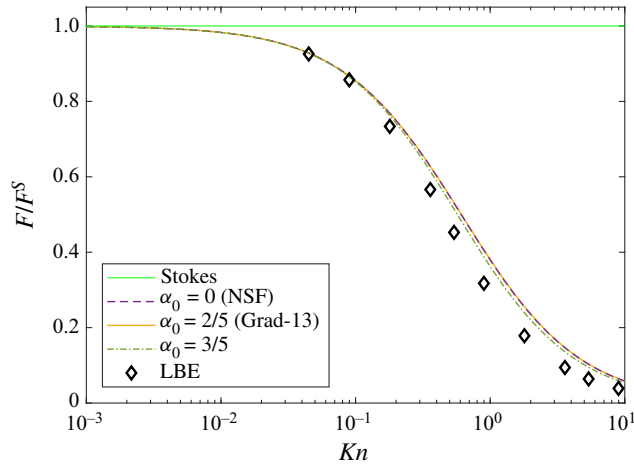


Figure 6. The normalised drag force on a liquid droplet versus Knudsen number. The results computed from the CCR–MFS, with  $\alpha_0 = 0$  (NSF),  $\alpha_0 = 2/5$  (Grad-13) and  $\alpha_0 = 3/5$  are compared with LBE data (symbols) of Sone, Takata & Wakabayashi (1994).

Curiously, all theories, except for that of Stokes, give reasonably accurate results. Note that, in this case, the net mass and heat flux from the droplet are zero with evaporation on the front side of the sphere and condensation on the back.

The problems considered in previous sections typically allow for analytic solutions, which are often not available for various practical problem of interest. In the following sections, we develop cases of increasing complexity, starting first with the motion over two particles at a finite distance from each other.

### 6.2. Motion over two solid spheres

Let us consider a flow over two solid spheres of equal radius with both fixed in shape and size. The flow is characterised by the following parameters: radii of the spheres (i.e. the Knudsen number), centre-to-centre distance  $2l_C$  and the angle  $\vartheta$  between the flow direction and the centreline; see figure 7.

For an axisymmetric case ( $\vartheta = 0$ ), the theoretical result for the drag force (which is equal for both the spheres) calculated by Stimson, Jeffery & Filon (1926) reads

$$F^S = -6\pi Kn u_\infty \beta, \tag{6.8}$$

where  $\beta$  is a correction coefficient which may be written in the form

$$\beta = \frac{4}{3} \sinh \alpha \sum_{k=1}^{\infty} \frac{n(n+1)}{(2n-1)(2n+3)} \left( 1 - \frac{4 \sinh^2 \left( n + \frac{1}{2} \right) \alpha - (2n+1)^2 \sinh^2 \alpha}{2 \sinh (2n+1) \alpha + (2n+1) \sinh 2\alpha} \right), \tag{6.9}$$

with  $\alpha = \cosh l_C$ .

In figure 8(a), the drag force (normalised with Stokes’ drag (6.7) for the single sphere) for an axisymmetric case ( $\vartheta = 0$ ) is plotted as a function of centre-to-centre distance for different values of the Knudsen number. The results from Stimson *et al.* (1926), which are only valid in the limiting case  $Kn \rightarrow 0$ , are included for comparison ( $\diamond$ ), and as expected,

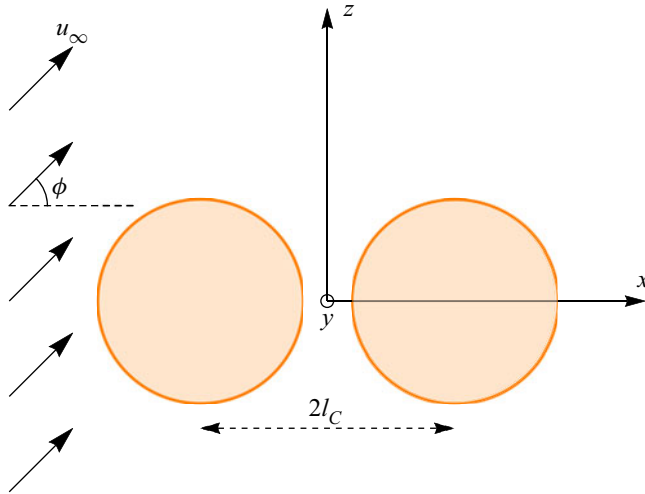


Figure 7. Schematic for the flow around two solid spheres. Here,  $2l_C$  is the centre-to-centre distance and  $\phi$  is the angle between flow direction and the line joining the centres.

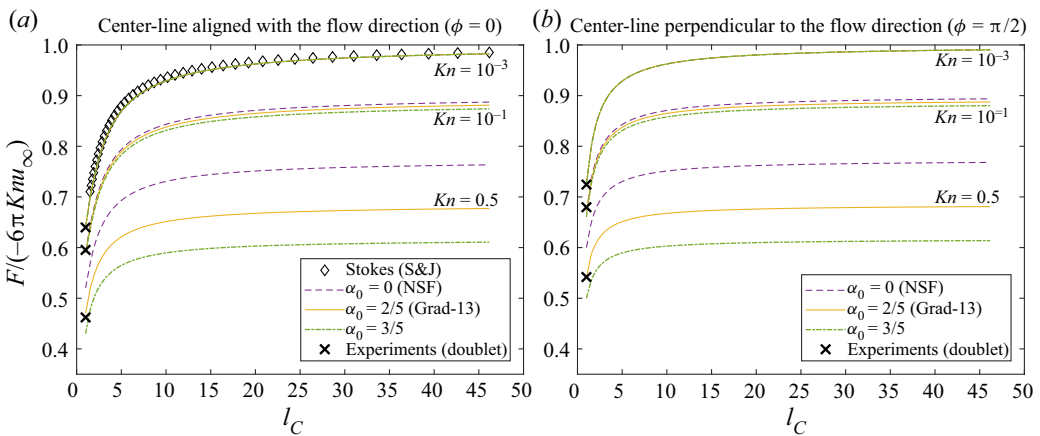


Figure 8. The drag force on two equal spheres versus centre-to-centre distance: (a) flow direction parallel to their line of centres and (b) flow direction perpendicular to their line of centres. The results computed from the CCR–MFS, with  $\alpha_0 = 0$  (NSF),  $\alpha_0 = 2/5$  (Grad-13) and  $\alpha_0 = 3/5$  are compared with the Stokes solution ( $\diamond$ ) derived by Stimson *et al.* (1926). The experimental results (denoted by  $\times$ ) for a doublet ( $l_C = 1/2$ ) obtained by Cheng *et al.* (1988) are included for comparison.

for small values of Knudsen number ( $Kn = 10^{-3}$ ), our results match with Stimson *et al.* (1926). The experimental results for  $l_C = 1/2$  obtained by Cheng *et al.* (1988) (and given by the empirical formula (6.10)) for  $Kn = 10^{-3}$ ,  $10^{-1}$  and 0.5 are also included ( $\times$ ) for comparison. For small Knudsen numbers ( $Kn \lesssim 10^{-1}$ ), all models (NSF, Grad-13, CCR) agree, whereas at large Knudsen numbers these are markedly different, with the NSF model over-predicting the drag compared with Grad-13 and CCR with  $\alpha_0 = 3/5$ . The effect of proximity is clearly visible on drag force, which decreases as  $l_C$  is reduced (i.e. the spheres get closer). Furthermore, in the limit  $l_C \rightarrow \infty$  the drag approaches that of the single sphere case (cf. figure 5). In addition, as with the case of a single sphere (cf.

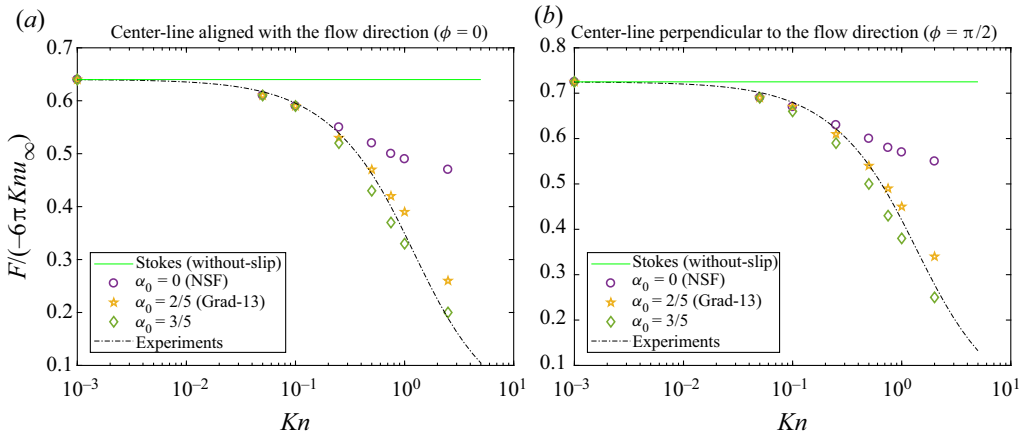


Figure 9. The drag force on a doublet: (a) flow parallel to its line of centres (axisymmetric case) and (b) flow perpendicular to its line of centres (non-axisymmetric case). The experimental data are taken from the empirical formula (6.10) obtained in Cheng *et al.* (1988).

figures 5 and 8a), the force monotonically decreases with increases in Knudsen number, for all models.

For the non-axisymmetric case ( $\phi = \pi/2$ ), the normalised drag force is plotted in figure 8(b) as a function of  $l_C$ , with  $Kn = 10^{-3}$ ,  $10^{-1}$  and 0.5. The experimental results of Cheng *et al.* (1988) for a doublet ( $l_C = 1/2$ ) are denoted by symbols ( $\times$ ). The overall drag force in the non-axisymmetric case is higher compared with the axisymmetric case (cf. figure 8a,b) and as before, the NSF theory over-predicts the drag.

### 6.2.1. Drag on a doublet

An interesting case arises when one considers  $l_C \rightarrow 1/2$ , i.e. when both spheres are in contact with one another, known as a doublet. Cheng *et al.* (1988) carried out experiments to study the effects of orientation (modulated by an electric field) on the measured drag force.

Figure 9 shows a comparison of the different models, computed using CCR–MFS, over a wide range of the Knudsen number. Here, the experimental data for the drag force acting on a doublet are taken from the empirical formula from Cheng *et al.* (1988), as

$$F = -\frac{4\pi Knu_\infty}{2^{1/3}} \frac{\phi_0}{1 + \frac{Kn}{\phi_0} \left[ 1.142 + 0.558 \exp\left(-0.999 \frac{\phi_0}{Kn}\right) \right]}, \quad (6.10)$$

where  $\phi_0 = 1.21$  or  $\phi_0 = 1.37$  for flow moving in parallel ( $\phi = 0$ ) or in perpendicular ( $\phi = \pi/2$ ) direction to the centreline, respectively.

As shown in figure 9, reassuringly for  $Kn \rightarrow 0$ , the results converges to the without-slip solution of the Stokes equation. For larger values of the Knudsen number, the force decreases owing to slip, and as  $Kn \rightarrow \infty$ , it reaches a finite value for the NSF theory; while from (6.10) it vanishes. Remarkably, from the results of the Grad-13 and the CCR models, we find that the force indeed vanishes for large Knudsen numbers. The results obtained from the Grad-13 and CCR models are both in good agreement with the experimental results, a slightly better match at larger Knudsen number is obtained by the CCR with  $\alpha_0 = 3/5$ .

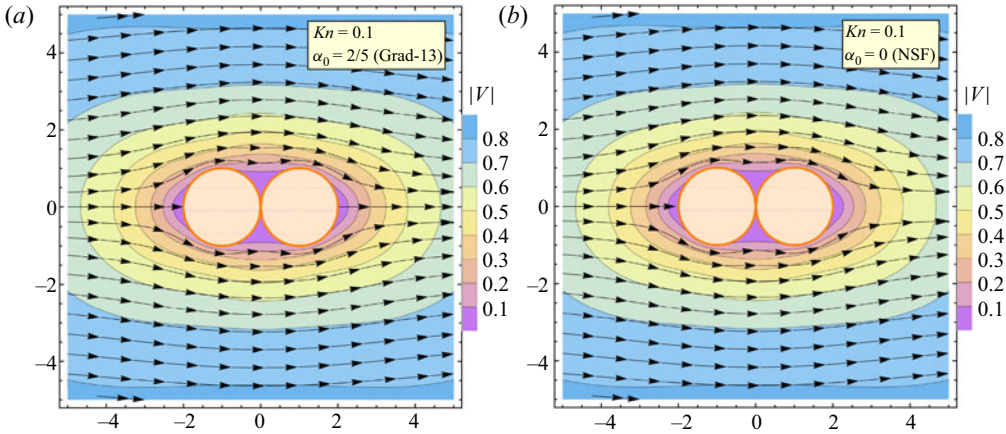


Figure 10. Streamlines and speed contours from the (a) Grad-13 and (b) NSF equations for Knudsen number 0.1: flow over a doublet with flow direction along the centreline ( $\phi = 0$ ). Vertical and horizontal axes represent  $x$ - and  $y$ -directions ( $N_c = N_s = 650$  and  $\gamma = R_s/R_c = 0.1$ ).

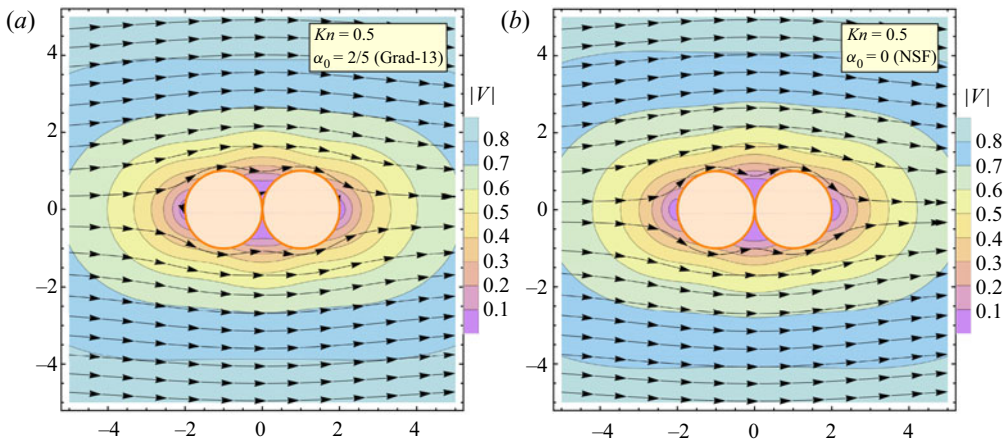


Figure 11. Streamlines and speed contours from the (a) Grad-13 and (b) NSF equations for Knudsen number 0.5: flow over a doublet with flow direction along the centreline ( $\phi = 0$ ). Vertical and horizontal axes represent  $x$ - and  $y$ -directions ( $N_c = N_s = 650$  and  $\gamma = R_s/R_c = 0.1$ ).

Figures 10 and 11 show the streamlines and the speed contours for the case  $Kn = 0.1$  and  $Kn = 0.5$ , respectively. The horizontal and vertical axes represent  $x$ - and  $z$ -axis, respectively, with flow in the  $x$ -direction. The left-hand side of these figures shows the Grad-13 ( $\alpha_0 = 2/5$ ) results for the case  $\phi = 0$ , and the right-hand side shows the results computed from the NSF ( $\alpha_0 = 0$ ) equations. Owing to the linearity of the equations, the speed contours are symmetric about the  $x = 0$  plane, resulting in equal drag forces on both spheres.

These contours show that, as to be expected, the slip velocity at the bottom and top surfaces increases with Knudsen number, resulting in reduced drag forces. For  $Kn = 0.1$  (figure 10), the flow line pattern predicted by the Grad-13 (a) and NSF (b) are very similar. The slip velocity is maximum near the top and bottom surface, which is virtually the same for the NSF and Grad-13 theories, thus giving similar predictions for the drag



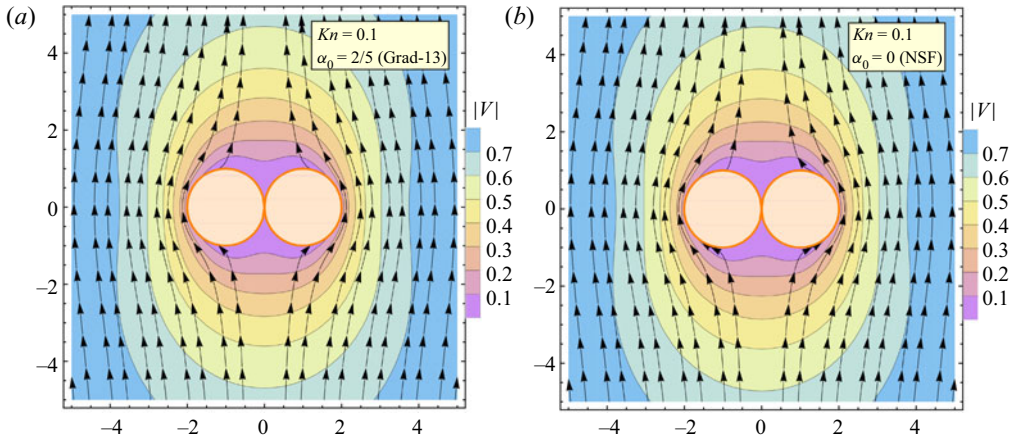


Figure 12. Streamlines and speed contours from the (a) Grad-13 and (b) NSF equations for Knudsen number 0.1: flow over a doublet with flow direction perpendicular to the centreline ( $\vartheta = \pi/2$ ). Vertical and horizontal axes represent  $x$ - and  $y$ -directions ( $N_c = N_s = 650$  and  $\gamma = R_s/R_c = 0.1$ ).

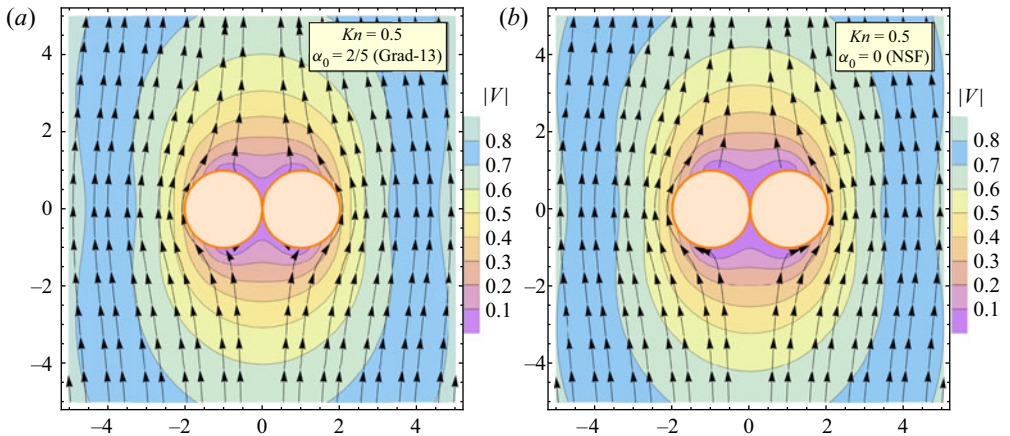


Figure 13. Streamlines and Mach contours from the (a) Grad-13 and (b) NSF equations for Knudsen number 0.5: flow over a non-evaporative ( $\vartheta = 0$ ) doublet with flow direction perpendicular to the centreline ( $\vartheta = \pi/2$ ). Vertical and horizontal axes represent  $x$ - and  $y$ -directions ( $N_c = N_s = 650$  and  $\gamma = R_s/R_c = 0.1$ ).

reduction (cf. figure 8). However, for  $Kn = 0.5$  (figure 11), the Grad-13 theory predicts a larger slip and thus greater drag reduction. The results from the CCR with  $\alpha_0 = 3/5$  are similar to those obtained from the Grad-13 theory, hence these are not shown here.

In figures 12 and 13, we again show the streamlines and speed contours predicted by both theories at  $Kn = 0.1$  and  $Kn = 0.5$ , respectively, for the case when flow (in the  $z$ -direction) is in a perpendicular direction to the centreline, i.e.  $\vartheta = \pi/2$ . Unlike the previous case, this is a truly three-dimensional set-up, where no symmetry exists in the azimuthal direction, with the MFS it is remarkably simple to solve this fully three-dimensional flow. The slip velocity increases with increasing the Knudsen number thus reducing the drag coefficient.



## Non-classical liquid–vapour phase-transition flows

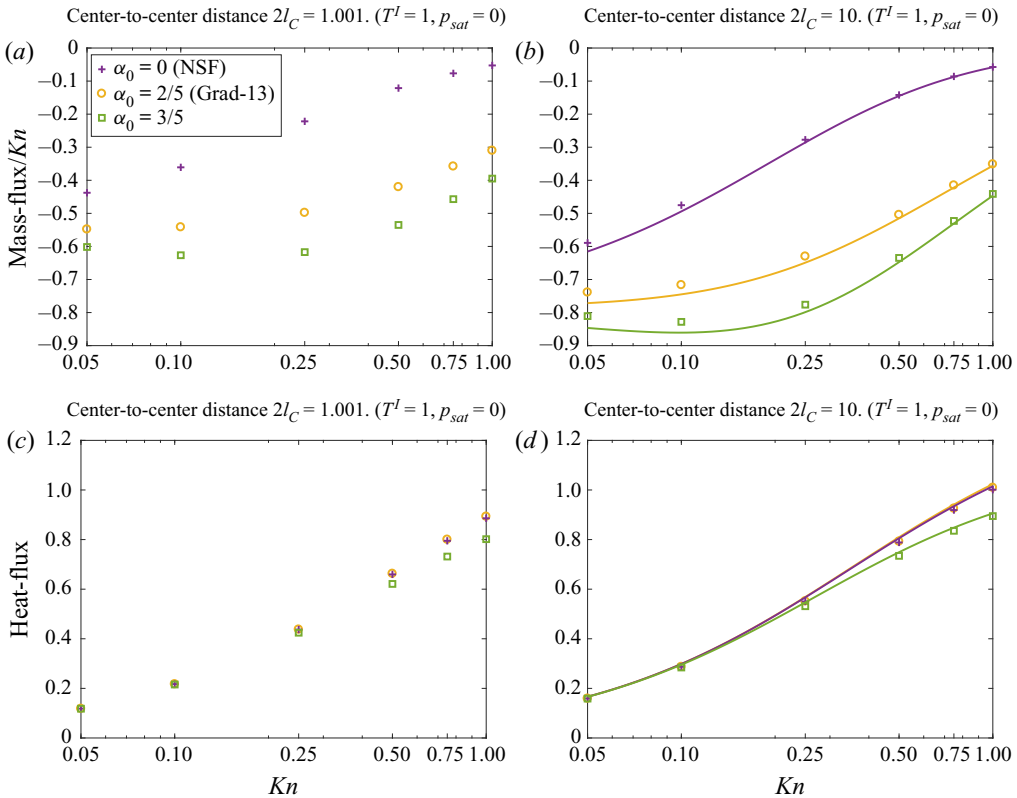


Figure 14. Two interacting droplets for the temperature-driven case ( $T^I = 1, p_{sat} = 0$ ): profiles of the (a) mass flux with centre-to-centre distance  $2l_C = 0.001$ , (b) mass flux with  $2l_C = 10$  (c) heat flux with  $2l_C = 0.001$  and (d) heat flux with  $2l_C = 10$  as functions of the Knudsen number for NSF, Grad-13 and CCR with  $\alpha_0 = 3/5$ . Symbols denote MFS and curves represent analytic solution from a single droplet.

### 6.3. Interaction of two evaporating droplets

The evaporation dynamics of two interacting droplets suspended in vapour will be investigated here; a problem relevant to dense-spray applications. We consider two droplets placed in a saturated vapour with centre-to-centre distance  $2l_C$ . Again, we consider the shape, size and the surface temperature of the droplet to be fixed.

As before, we consider two cases, i.e. (i) evaporation is driven by temperature difference (i.e.  $p_{sat} = p_\infty = 0$  and  $T^I = 1$ ) and (ii) evaporation owing to pressure difference ( $p_{sat} = 1$  and  $T^I = T_\infty = 0$ ). The distance between the two droplets and the value of the Knudsen number are varied in order to investigate the proximity and rarefaction effects. The results from three models are compared with the NSF, Grad-13 and CCR with  $\alpha_0 = 3/5$ .

*Temperature-driven case:* In figure 14, we show the mass flux and the heat flux per unit area as a function of Knudsen number for the temperature-driven case. The mass flux reduces monotonically with the Knudsen number whereas the NSF theory predicts a higher mass flux than the CCR. Figures 14(a) and 14(b) illustrate the mass flux with centre-to-centre distance  $2l_C = 0.001$  (i.e. when the droplets are next to each other) and  $2l_C = 10$  (i.e. at a distance where proximity effects are negligible), respectively. The corresponding heat flux is shown in figures 14(c) and 14(d).

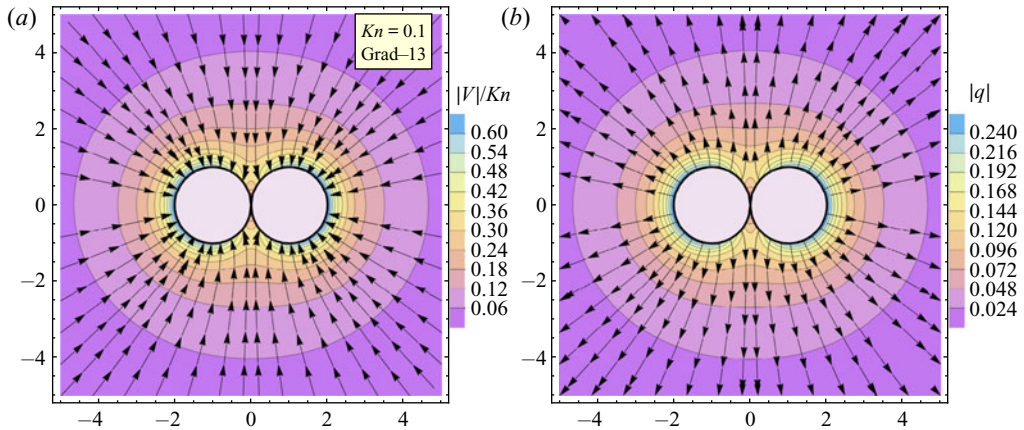


Figure 15. Two droplets placed adjacent to each other ( $2l_c = 1.001$ ) for the temperature-driven case ( $T^l = 1$ ,  $p_{sat} = 0$ ): (a) streamlines and speed contours and (b) heat-flux lines and magnitude, obtained from the Grad-13 MFS. Vertical and horizontal axes represent  $x$ - and  $y$ -directions ( $N_c = N_s = 650$  and  $\gamma = R_s/R_c = 0.1$ ).

When the droplets are next to each other a shielding effect is observed, and, as a result, the mass flux reduces (cf. figure 14a,b). At  $Kn = 0.05$ , all three models predict approximately 29% reduction in the mass flux as compared with a single droplet (i.e.  $l_c \rightarrow \infty$ ). The reduction in the mass flux decreases with increase in Knudsen number. For  $Kn = 1$ , NSF, Grad-13 and CCR with  $\alpha_0 = 3/5$  predicts approximately 9%, 13% and 12% reduction in mass flux, respectively.

The mass fluxes computed from the MFS (symbols) for centre-to-centre distance 10 are shown in figure 14(b). The analytic results from a single droplet are also plotted (continuous lines) for comparison. As expected, as the droplets are moved farther apart, the results converge to the single-droplet case; the mass flux is within 5% (for  $Kn = 0.05$ ) and 1% (for  $Kn = 1$ ) for the single-droplet case.

Similarly, the proximity effects on the heat flux are visible in figures 14(c) and 14(d), for  $2l_c = 0.001$  and  $2l_c = 10$ , respectively. Again, the heat flux reduces as  $l_c \rightarrow 1/2$ , and as the value for the Knudsen number increases the proximity effects diminish. The percentage difference in the heat flux from the single-droplet cases varies from approximately 29% to 12% for  $2l_c = 1.001$  and from approximately 4% to 1% for  $2l_c = 10$ , as the value of Knudsen number varies from 0.05 to 1.

The vapourisation dynamics of a pair of droplets placed adjacent to each other is markedly different from the single-droplet counterpart. In figure 15, (a) the streamlines superimposed on the velocity magnitude contours and (b) the heat-flux lines and the magnitude contours are shown. The heat leaves the hot droplets owing to negative temperature gradients while condensation occurs in order to compensate for the heat loss. Figure 15 shows that the mass flux and the heat flux at the confined region between the droplets are sufficiently lower than at the outer regions. In this region, the vapour temperature is relatively high, thus a smaller temperature jump which leads to a reduced mass flux and heat flux.

*Pressure-driven case:* In figure 16, we show (a) mass flux with centre-to-centre distance  $2l_c = 0.001$ , (b) mass flux with  $2l_c = 10$ , (c) heat flux with  $2l_c = 0.001$  and (d) heat flux with  $2l_c = 10$  as functions of the Knudsen number for the pressure-driven case. Again, in

## Non-classical liquid–vapour phase-transition flows

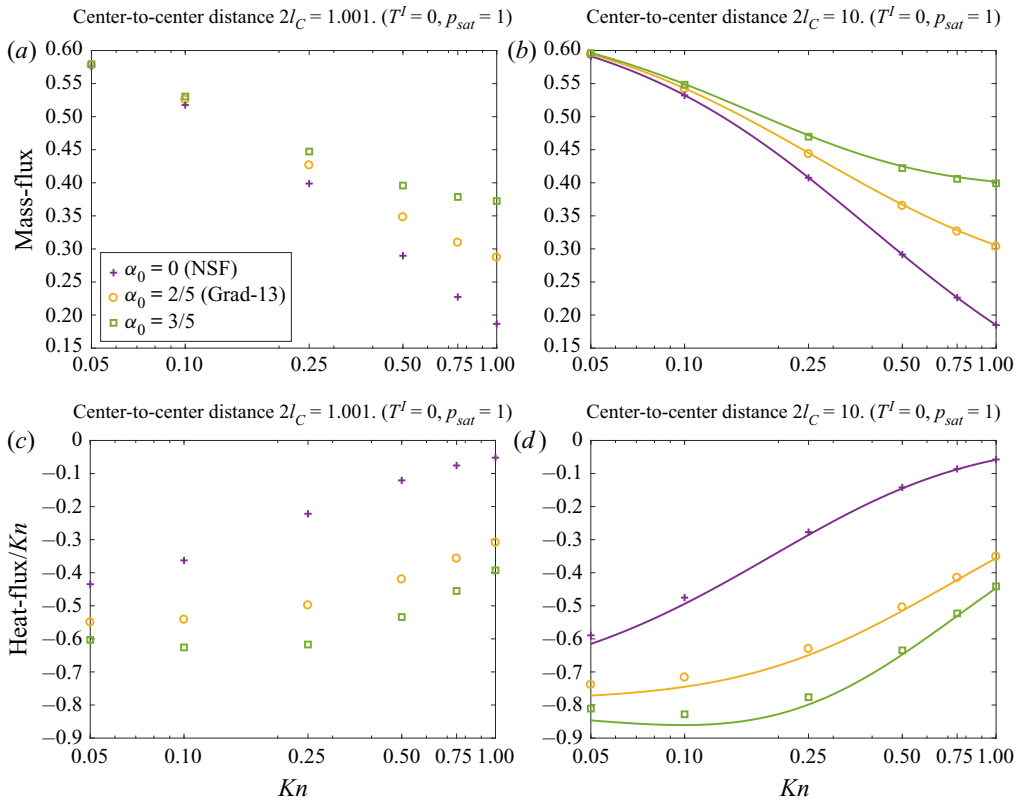


Figure 16. Two interacting droplets for the pressure-driven case ( $T^I = 0, p_{sat} = 1$ ): profiles of (a) mass flux with centre-to-centre distance  $2l_C = 0.001$ , (b) mass flux with  $2l_C = 10$ , (c) heat flux with  $2l_C = 0.001$  and (d) heat flux with  $2l_C = 10$  as functions of the Knudsen number for NSF, Grad-13 and CCR with  $\alpha_0 = 3/5$ . Symbols denote MFS and curves represent analytic solution from a single droplet.

order to gain insights into the proximity effects, the numerical solution obtained via the MFS (symbols) and the analytic results from a single-droplet case (continuous lines) are compared in figure 16. In this case, the mass flux is slightly reduced ( $\lesssim 3\%$  for  $2l_C = 0.001$  and  $\lesssim 0.06\%$  for  $2l_C = 10$ ) in the range ( $0.05 \leq Kn \leq 1$ ). On the other hand, the proximity effects on the heat flux are observed to be significant. For  $2l_C = 0.001$ , the magnitude of the heat flux is reduced approximately 29.3% for NSF (28.7% for Grad-13 and CCR) at  $Kn = 0.05$  and approximately 10% for NSF ( $\leq 15\%$  for Grad-13 and CCR) at  $Kn = 1$ . For  $2l_C = 0.001$ , all models give less than a 4% reduction in heat flux, for all ranges of Knudsen number considered.

Another interesting point to be noted from figure 16(c,d) is that the heat flux predicted by the NSF equations is significantly lower in magnitude compared with the CCR and Grad-13 models, especially in the transition regime ( $Kn \geq 0.1$ ). Within this regime, the heat flux is not only driven by the temperature gradient (i.e. Fourier's law) but also owing to the pressure gradient, this second-order effect can easily be understood from the constitutive relations (2.5a,b) and the momentum balance equation (2.4a–c), which give

$$\mathbf{q} = -\frac{c_p Kn}{Pr} (\nabla T - \alpha_0 \nabla p). \quad (6.11)$$

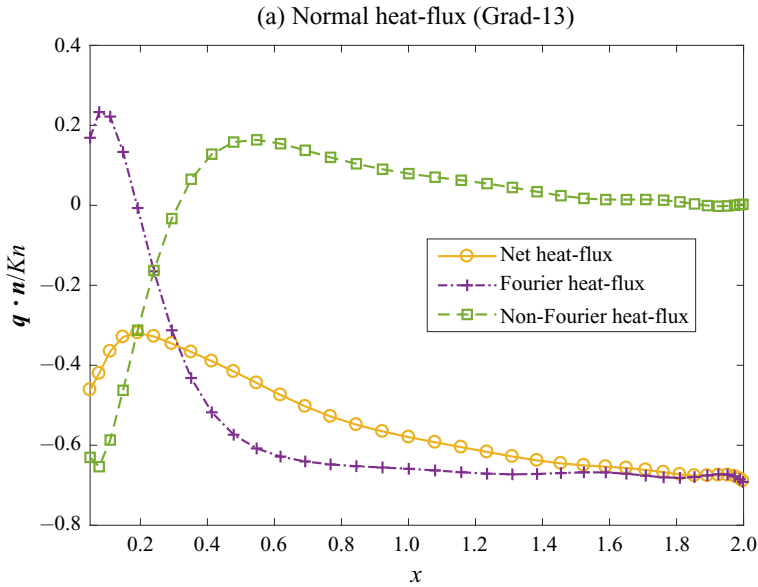


Figure 17. Two interacting droplets for the pressure-driven case ( $T^l = 0, p_{sat} = 1$ ): Fourier and non-Fourier contributions to the normal heat flux ( $\mathbf{q} \cdot \mathbf{n}/Kn$ ) given by the Grad-13 theory plotted along the top surface of the droplet in  $x$ - $z$  plane.

Here, the second term on the right-hand side is the non-Fourier contribution to the heat flux owing to pressure gradient (Rana *et al.* 2018a). In figure 17, we show two different contributions to the scaled normal heat flux ( $\mathbf{q} \cdot \mathbf{n}/Kn$ ) along the surface of the droplet (in the  $x$ - $z$  plane) for the pressure-driven case with  $Kn = 0.1$ . As predicted from the Grad-13 theory, the heat flux owing to the pressure gradient (non-Fourier) and heat flux owing to the temperature gradient (Fourier) have opposing effects, and consequently the net heat flux is reduced in the second-order theories.

In figure 18, we again show the streamlines and the velocity magnitude contours (a), and the heat-flux lines and the magnitude contours (b) for the pressure-driven case. In this case, evaporation occurs owing to a negative pressure gradient and the heat flows inwards. The mass flux and the heat flux at the confined region between the droplets are reduced owing to a high vapour pressure.

The high-pressure region created between two droplets pushes them away from each other. The net drag force (in the  $x$ -direction) acting on each droplet is plotted in figure 19 as a function  $Kn$ . The results for various values of centre-to-centre distance shown in figure 19 are computed from the Grad-13 model, the drag force predicted by the NSF model is within 10% and not shown. The force decreases exponentially as droplets become farther apart, i.e. as  $l_C$  increases. Interestingly, the drag force attains a minimum value at a certain Knudsen number, which depends on how far the droplets are from each other. As  $Kn \rightarrow \infty$ , the drag force vanishes.

#### 6.4. Evaporation of a deformed droplet

In this section, we study evaporation/condensation from a deformed droplet with a fixed shape and size, in order to gain some initial insight into evaporation occurring during

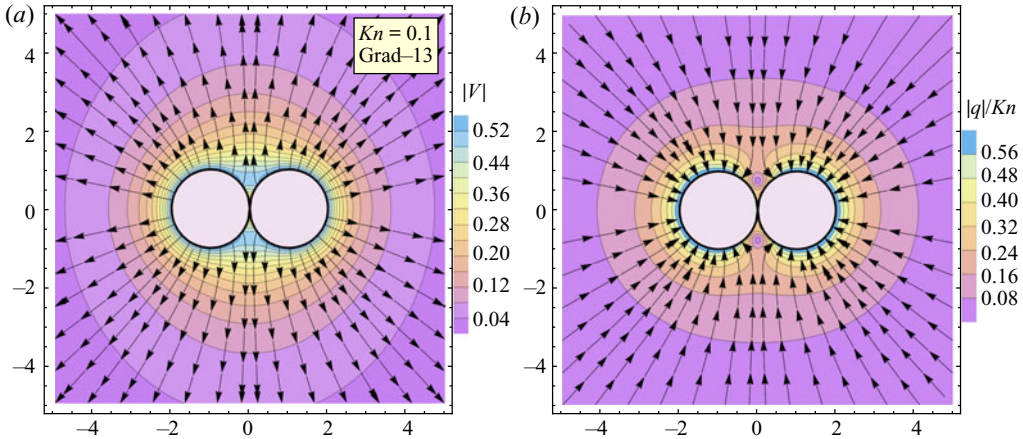


Figure 18. Two droplets placed next to each other ( $2l_c = 1.001$ ) for the pressure-driven case ( $T^I = 0, p_{sat} = 1$ ): (a) stream lines and speed contours (b) heat-flux lines and magnitude, obtained from the Grad-13 MFS. Vertical and horizontal axis represent  $x$ - and  $y$ -directions. ( $N_c = N_s = 650$  and  $\gamma = R_s/R_c = 0.1$ ).

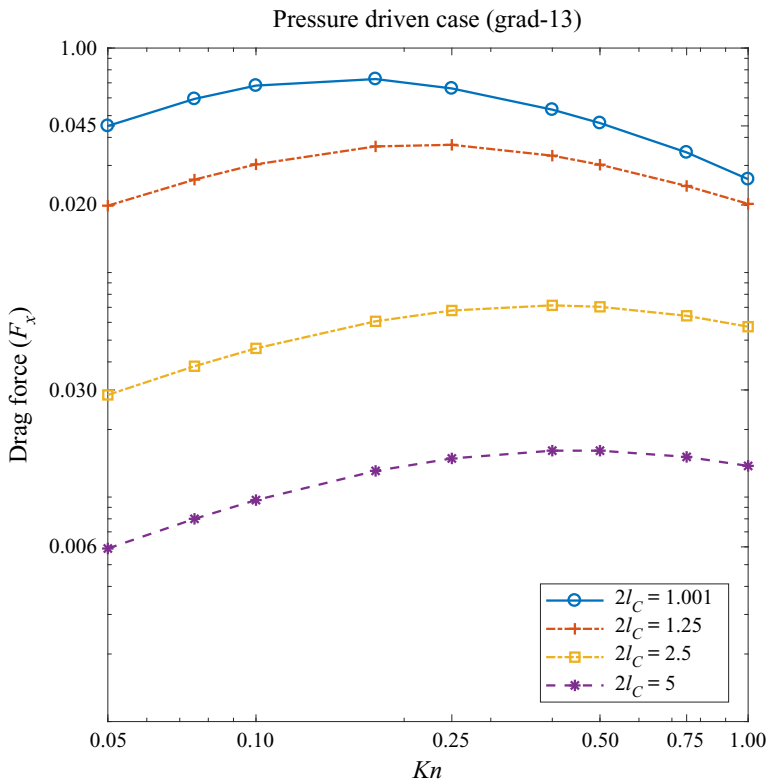


Figure 19. The drag force acting on the droplets versus Knudsen numbers for various values of the separation distance as predicted by the Grad-13 theory for the pressure-driven case.

oscillatory and/or deformed droplet events, leaving the step to unsteady flow as a focus for future work. The effects of heat conduction and the flow inside the droplet are not considered. The parametric equation for the droplet surface in the second harmonic mode is given by (see, e.g., Sprittles & Shikhmurzaev 2012)

$$X = \eta_0 \left[ 1 + \frac{\eta}{2} (3 \cos^2 \phi - 1) \right] \{ \sin \phi \cos \theta, \sin \phi \sin \theta, \cos \phi \}, \quad (6.12)$$

where  $\phi \in [0, \pi]$ ,  $\theta \in [0, 2\pi]$  and  $\eta$  is the shape factor. The volume of the droplet is

$$V = \eta_0 \frac{4\pi}{3} \left( \frac{35 + 21\eta^2 + 2\eta^3}{35} \right)^{1/3}. \quad (6.13)$$

Therefore, in order to have the volume  $V$  equal to a spherical droplet of radius 1, the normalising factor  $\eta_0$  is given by

$$\eta_0 = \left( \frac{35}{35 + 21\eta^2 + 2\eta^3} \right)^{1/3}. \quad (6.14)$$

The droplet shapes with different values of shape parameter  $\eta = 0, 0.5$  and  $1$  are depicted in figure 20; the corresponding (non-dimensional) surface area of the droplets are  $4\pi$ ,  $4\pi \times 1.078$  and  $4\pi \times 1.192$ , respectively.

We shall again consider two cases: (i) flow caused by a unit pressure difference while the temperature of the liquid is equal to the far-field temperature (i.e.  $p_{sat} - p_\infty = 1$  and  $T^l - T_\infty = 0$ ) and (ii) flow caused by a unit temperature difference while the saturation pressure in the liquid is same as the far-field pressure (i.e.  $p_{sat} - p_\infty = 0$  and  $T^l - T_\infty = 1$ ).

*Pressure-driven case:* In figure 21(a–c), we show the mass flux per unit area as a function of  $Kn$  computed using the NSF, Grad-13 and  $\alpha_0 = 3/5$  models, respectively for the shape parameter  $\eta = 0, 0.5$  and  $1$ . Here, the numerical results from the MFS are denoted by symbols and the analytic results for the spherical droplet ( $\eta = 0$ ) are represented by the solid line. For small deformity ( $\eta = 0, 0.5$ ), the mass flux is nearly same, however when the droplet is more deformed ( $\eta = 1$ ) the mass flux is reduced. The percentage reduction in the mass flux (compared with a spherical droplet) is approximately 11 % for  $Kn = 0.05$  and approximately 21 % for  $Kn = 1$ . In a similar manner to the case of two droplets placed next to each other, considered in the previous section, the reduction in the mass flux is caused by the formation of a high pressure in the high curvature (for  $\eta = 1$ ) cusp region near  $z = 0$ , which is not present at smaller  $\eta$ .

Similarly, in figure 22(a–c) we plot the heat flux per unit area as a function of  $Kn$  for the same shape parameters. Note that the heat flux owing to pressure difference is a first-order quantity in terms of  $Kn$  (that is, it vanishes as  $Kn \rightarrow 0$ ), hence in these figures we have scaled the heat flux with inverse  $Kn$ . Again, the heat-flux magnitude reduces as  $\eta \rightarrow 1$ . The reduction in the heat flux is approximately 13 %. Furthermore, the Grad-13 and CCR theories predict a larger heat flux compared with the NSF results owing to non-Fourier heat-flux contribution (6.11).

*Temperature-driven case:* In figure 23, we present the heat flux per unit area for the temperature-driven case for different shape factors (see legend in the figures) for NSF (a), Grad-13 (b) and CCR with  $\alpha_0 = 3/5$  (c). Note that, owing to the Onsager reciprocity relations (Chernyak & Margilevskiy 1989), the mass flux for the temperature-driven case is the same as the heat flux for the pressure-driven case (figure 22), hence it is not shown.



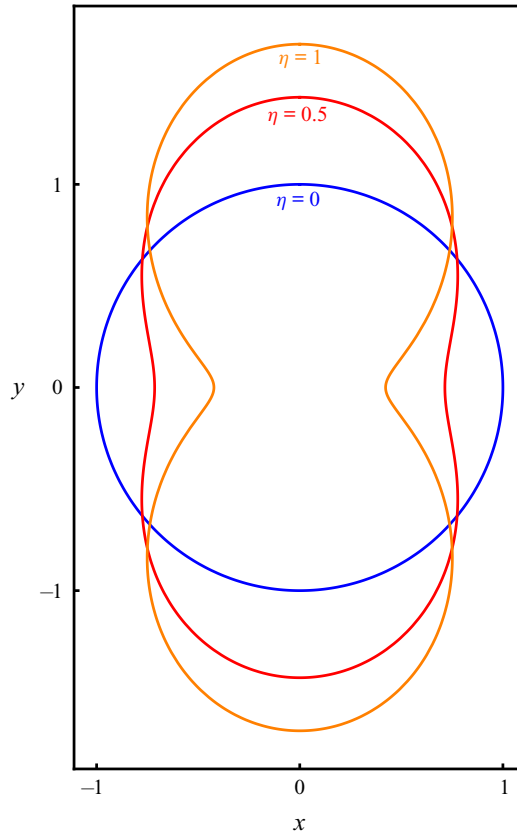


Figure 20. Droplet shapes given by second spherical harmonics with shape parameter  $\eta = 0, 0.5$  and  $1$  and the normalising factor  $\eta_0 = 35^{1/3}/(35 + 21\eta^2 + 2\eta^3)^{1/3}$  ensuring that the droplet has fixed volume.

Evidently, from figure 23, the magnitude of the heat flux reduces with the deformation, i.e. as  $\eta \rightarrow 1$ . For NSF (figure 23a), the reduction is approximately 3% for  $\eta = 0.5$  and approximately 12% for  $\eta = 1$ .

*Curvature dependence of the saturation pressure:* Throughout this paper, we have taken  $T^I$  and  $p_{sat}$  as independent parameters. However, in general, the Clausius–Clapeyron–Kelvin formula provides a relation between the saturation pressure and the temperature at the interface (linearised and dimensionless) (McElroy 1979; Bond & Struchtrup 2004):

$$p_{sat}(T^I) = p_{sat}^p(T^I) \underline{\exp(2\gamma\kappa)}. \quad (6.15)$$

Here,  $\gamma$  is the dimensionless surface tension ( $\gamma = \hat{\gamma}/\hat{\rho}_l \hat{\ell} \hat{R} \hat{T}_0$ ),  $\kappa$  is the dimensionless curvature ( $\kappa = \hat{\kappa} \hat{\ell}$ ) and  $p_{sat}^p(T^I) = H_0 T^I$  is the saturation pressure for a planar surface with  $H_0 (= \hat{H}_0/\hat{R} \hat{T}_0)$  being the dimensionless heat of evaporation.

Thus far, the modelling assumption has been that  $H_0$  (and  $\gamma$ ) can be independently chosen to give a desired value of the saturation pressure. Notably, for the noble gases (vapour/liquid) the Kelvin correction term (underlined) in (6.15) are often small, unless the radius of curvature  $\hat{\kappa}$  is in nanometers. For example, for argon, if we choose  $\hat{T}_0 = 103$  K,  $\hat{p}_0 = p_{sat}^p(\hat{T}_0) = 0.4$  MPa,  $\hat{\rho}_l = 1294.6$  kg m<sup>-3</sup> and  $\hat{\gamma} = 8.75$  mN m<sup>-1</sup> (a case

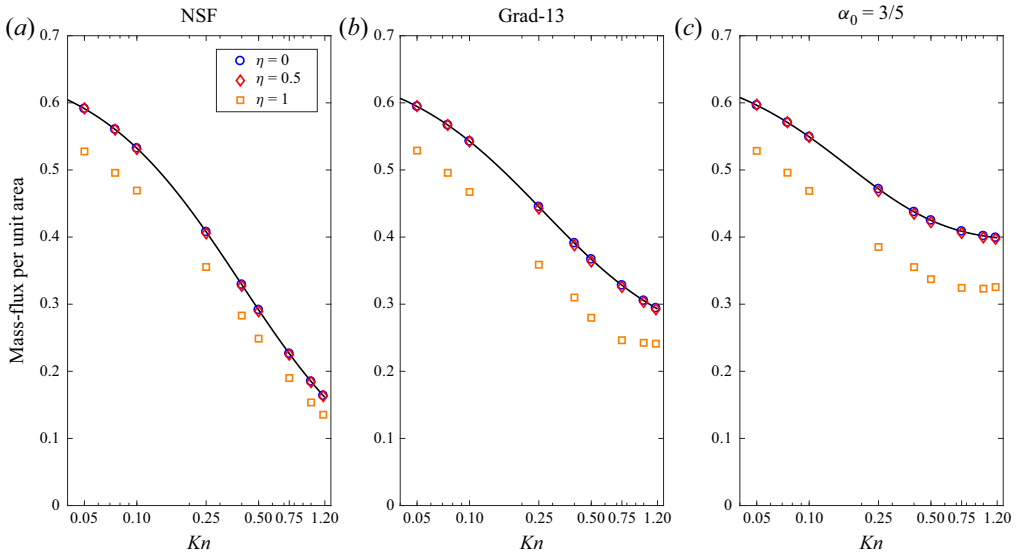


Figure 21. Pressure-driven case ( $p_{sat} - p_\infty = 1$ ,  $T^l - T_\infty = 0$ ); mass flux per unit area versus Knudsen number with  $\eta = 0, 0.5$  and  $1$ : (a) NSF, (b) Grad-13 and (c)  $\alpha_0 = 3/5$ . The symbols denote the MFS and the solid lines represent analytic results for a spherical droplet.

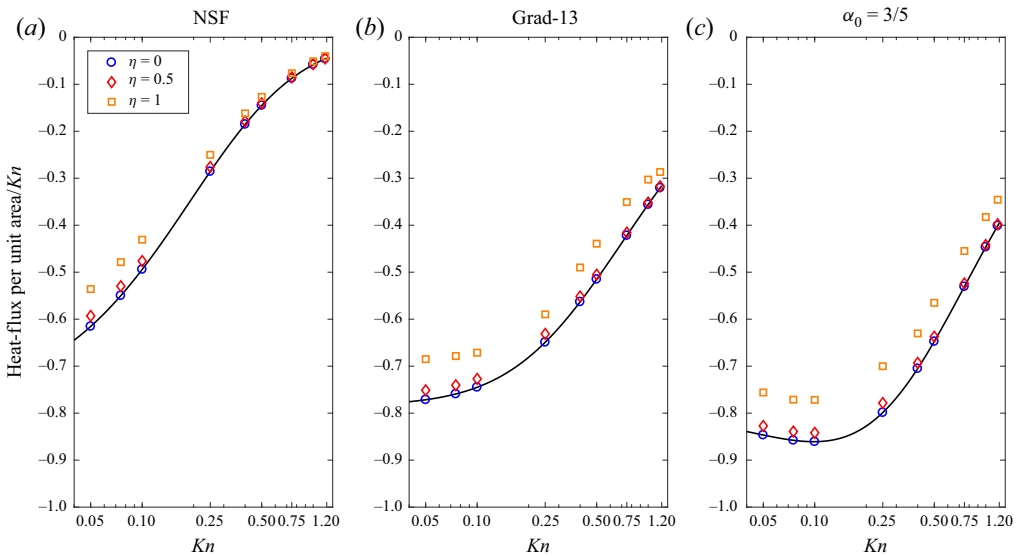


Figure 22. Pressure-driven case ( $p_{sat} - p_\infty = 1$ ,  $T^l - T_\infty = 0$ ); heat flux per unit area/ $Kn$  versus Knudsen number with  $\eta = 0, 0.5$  and  $1$ : (a) NSF, (b) Grad-13 and (c)  $\alpha_0 = 3/5$ . The symbols denote the MFS and the solid lines represent analytic results for a spherical droplet.

considered in Rana *et al.* 2019), the Kelvin correction term gives  $\exp(0.6305/a)$ , where  $a$  (in nanometres) is the inverse of local curvature  $\hat{\kappa}$ . Therefore, for a drop of size greater than 10 nm, the effect of the Kelvin correction term will be less than 6.1 %.

In order to compare our results with existing literature, in § 7 we use the dimensionless heat of evaporation  $H_0$  as an independent parameter.

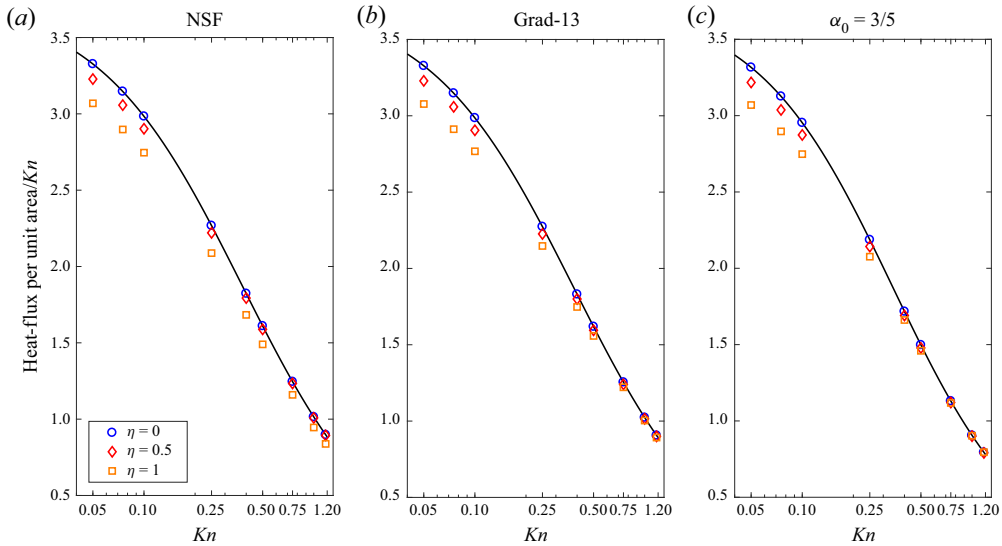


Figure 23. Temperature-driven case ( $p_{sat} - p_{\infty} = 0, T^l - T_{\infty} = 1$ ); heat flux per unit area/ $Kn$  versus Knudsen number with  $\eta = 0, 0.5$  and  $1$ : (a) NSF, (b) Grad-13 and (c)  $\alpha_0 = 3/5$ . The symbols denote the MSF solutions and the solid lines represent analytic results for a spherical droplet.

### 7. Inverted temperature profile and Knudsen layer

A notorious deficiency of the NSF and CCR theories is their inability to capture the Knudsen layer, a kinetic boundary layer extending within a few mean free paths into the domain (Sone 2007; Struchtrup & Torrilhon 2008; Torrilhon 2016). We have seen in previous sections that the CCR model is able to predict global flow features, such as net mass flux, heat flux and drag, however, it may fail to describe finer flow features, especially those in which the Knudsen layer and other rarefaction effects are dominant. In this section, we consider such a case.

Let us consider heat and mass transfer between two liquid layers located at locations  $x = \pm 1/2$ , see figure 24. We prescribe the dimensionless temperature and saturation pressure of the liquid layers as  $T^l(\pm 1/2) = \pm \Delta\theta$  and  $p_{sat}(\pm 1/2) = \pm \Delta p$ . For a planar surface,  $\hat{k} = 0$ , and thus  $\Delta p = \Delta\theta H_0$ .

After some calculation, the analytic solution of the linear problems (2.4a–c) and (2.5a,b) assumes the form

$$v_x = c_1, \quad q_x = c_2, \quad T = -\frac{Pr c_2}{c_p Kn} x, \tag{7.1a}$$

$$p = \sigma_{xx} = 0, \tag{7.1b}$$

where  $c_1$  and  $c_2$  are integration constants, which need to be evaluated using boundary conditions. Solving (4.2) for  $c_1$  and  $c_2$  gives

$$c_1 = \sqrt{\frac{2}{\pi}} \left( \frac{(0.306763 + 1.62499Kn)H_0 - 0.741358Kn}{0.370583 + 1.77245Kn} \right) \Delta\theta, \tag{7.2a}$$

$$c_2 = \frac{5Kn}{2Pr} \left( \frac{0.741165 - 0.157738H_0}{0.370583 + 1.77245Kn} \right) \Delta\theta. \tag{7.2b}$$

Note that, for this problem, the CCR reduces to the NSF constitutive relations.

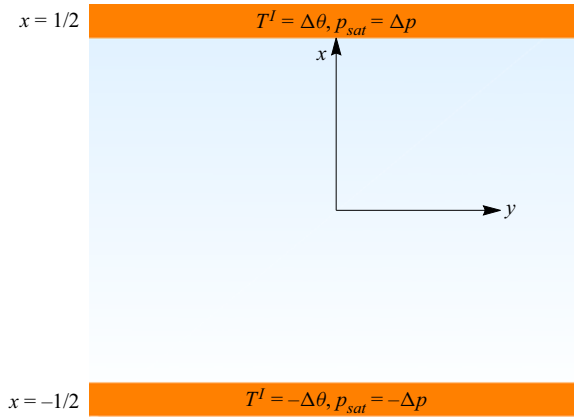


Figure 24. Schematic for heat and mass transfer between two liquid layers.

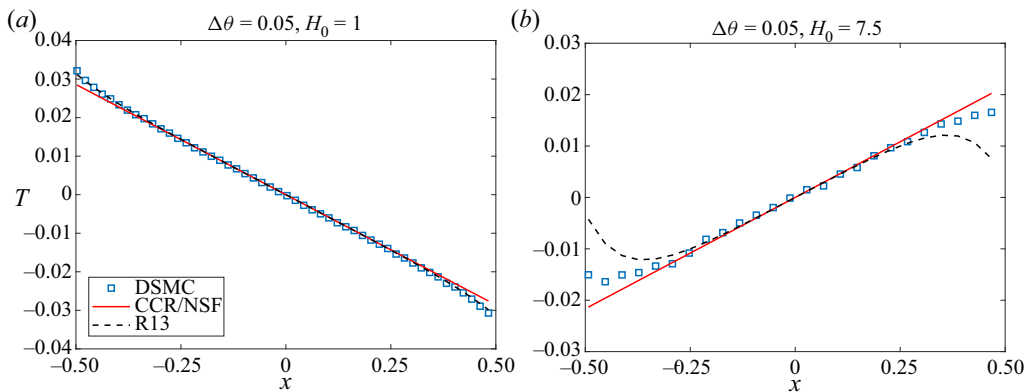


Figure 25. Temperature profiles as functions of location  $x$  for (a) ( $\Delta\theta = 0.05, H_0 = 1$ ) and (b) ( $\Delta\theta = 0.05, H_0 = 7.5$ ) for  $Kn = 0.078$ . The figure on the right shows the inverted temperature profile.

Interestingly, as can be seen from inspection of (7.2b), the conductive heat flux  $q_x$  switches sign for  $H_0 \geq 4.7$ , which leads to an inverted temperature profile in the vapour, this is qualitatively consistent with kinetic theory (Pao 1971) and MD simulations (Frezzotti, Grosfils & Toxvaerd 2003). Notably, the NSF equations with classical boundary conditions, i.e. with no temperature-jump boundary conditions, along with the Hertz–Knudsen–Schrage, can not describe the inverted temperature phenomenon.

Figures 25(a) and (b) show the temperature curves as functions of  $x$  for  $\Delta\theta = 0.05, H_0 = 1 (<4.7)$  and  $\Delta\theta = 0.05, H_0 = 7.5 (>4.7)$ , respectively, for  $Kn = 0.078$ . These flow parameters are chosen so that our results can be compared with those obtained from the direct simulation Monte Carlo (DSMC) and R13 theories given in Beckmann *et al.* (2018). Comparing both cases, when  $H_0$  is smaller than the critical heat of evaporation (case 1) the temperature profile shows a large jump at both boundaries with higher temperature on the lower boundary. In this case, the mass and heat fluxes are both positive (i.e. from lower boundary to upper) and as expected, the temperature is higher at the lower boundary. On the other hand, in case 2,  $H_0$  is larger than the critical heat of evaporation and the temperature profile is inverted. For this case the heat flows from the hot side (where

condensation occurs) towards the cold side (where evaporation occurs). The results from the DSMC are denoted by symbols.

Evidently, the CCR theory qualitatively explains the intriguing inverted temperature phenomenon. However, the CCR model does not provide detail of the temperature profiles near to the boundaries, the region which is dominated by the Knudsen layer. The R13 theory provides improvement in predicting the temperature profile at this value of the Knudsen number because, as is well known, it can capture some basic features of the Knudsen layer.

## 8. Conclusion and future directions

The present paper studies liquid–vapour phase-transition processes in which  $Kn \lesssim 1$ , i.e. down to sub-micrometre scales. In particular, we derive a set of fundamental solutions for the CCR system which allows for three-dimensional multiphase micro-flows at remarkably low computational cost, the fundamental solutions to the linearised NSF and Grad-13 equations are obtained as a special case. A set of thermodynamically consistent liquid–vapour interface conditions for the linearised CCR system are derived within the framework of irreversible thermodynamics.

Different macroscopic models were applied to solve the motion of a sphere in a gas and the results were compared with theoretical and experimental results from the literature. We observed that the results for the drag force obtained from the Grad-13 and CCR model are both in good agreement with the experimental results, a slightly better match at larger Knudsen number is obtained by taking  $\alpha_0 = 3/5$ .

The motion of two spherical particles was investigated and compared with the classical Stokes solutions and experimental results. The drag force reduces as the Knudsen number increases, mainly owing to velocity slip at the surface. The effect of proximity is investigated on the drag force, which decreases as the particles get closer. For a doublet, contrary to the experimental observations, the Stokes and NSF equations predict a non-zero drag whereas the Grad-13 and the CCR, with coupling coefficient  $\alpha_0 = 3/5$ , provide an excellent match with the experimental data. Proximity effects on mass and heat transfer coefficients of two interacting droplets were investigated over a range of Knudsen numbers. Two far-field conditions were examined, (i) pressure-driven, where  $p_{sat} - p_\infty = 1$ ,  $T^l - T_\infty = 0$ , and (ii) temperature-driven, where  $p_{sat} - p_\infty = 0$ ,  $T^l - T_\infty = 1$ . However, owing to the linearity of the governing equations and the boundary conditions involved, these two cases can be combined to give results for a general case. For the pressure-driven case a slight reduction ( $\lesssim 3\%$ ) in the mass flux was observed when the droplets are placed next to each other. On the other hand, the heat flux was significantly reduced ( $\sim 30\%$ ). For the temperature-driven case, the situation is reversed, where a significant reduction in the mass flux was observed owing to shielding effects. We also considered the case of a single deformed droplet and studied the effects of deformity on the mass- and heat-transfer characteristics over a range of the Knudsen number.

Motivated by these findings, future work could be to extend this work to study the phase-transition process in polyatomic fluids and binary mixtures.

Extension of the current work to unsteady flows and coupling to liquid dynamics (Rana *et al.* 2019; Chubynsky *et al.* 2020) can be considered in the future, the liquid phase can be modelled as an incompressible fluid (Stokeslet/Oseenlet and heatlet) and the vapour phase modelled via the CCR model. However, it will require solving the moving-boundary problem efficiently within the MFS framework (Jiang *et al.* 2014). Another line of inquiry

would be to implement these fundamental solutions via boundary integral methods which offer more flexibility and robustness as compared to the MFS. A prominent deficiency of the NSF and the CCR model is their inability to capture the Knudsen layer, a kinetic boundary layer extending a few mean free paths into the domain. Future work can also include finding fundamental solutions to the linearised R26 equations in order to incorporate Knudsen layers. The cornerstone of this work is the linearity of the differential operators involved, which allow us to obtain Green's functions and formulate the MFS. As such, the method developed here can not be directly applied to nonlinear problems. In another context, the MFS has been applied to some nonlinear problems using appropriate fixed-point iterative schemes (Fan, Chen & Monroe 2009). It would be interesting to attempt a similar approach for solution of the nonlinear CCR model and/or nonlinear boundary conditions.

**Funding.** This work has been partially supported via the Scheme for Promotion of Academic and Research Collaboration (SPARC) grant (IDN\_SKI 444) funded by the Ministry of Human Resources Development (MHRD), India and EPSRC Grant Numbers EP/N016602/1, EP/P031684/1 and EP/S029966/1. The authors are grateful to Dr J. Padrino from the University of Warwick for many fruitful discussions on Green's functions.

**Declaration of interests.** The authors report no conflict of interest.

**Author ORCIDs.**

- Anirudh S. Rana <https://orcid.org/0000-0002-5241-7102>;
- Suman Chakraborty <https://orcid.org/0000-0002-5454-9766>;
- Duncan A. Lockerby <https://orcid.org/0000-0001-5232-7986>;
- James E. Sprittles <https://orcid.org/0000-0002-4169-6468>.

**Appendix A. Derivation of the Green's functions for the Sourcelet**

The Fourier transformation of the energy conservation law (3.5a-c<sub>3</sub>) and the heat-flux constitutive relation (2.5a,b<sub>2</sub>) gives

$$k \cdot \tilde{q} = 0 \quad \text{and} \quad \tilde{q} = i \frac{c_p Kn}{Pr} k \tilde{\Theta}, \tag{A1a,b}$$

where we have defined  $\Theta = T - \alpha_0 p$  and its Fourier transformation  $\mathcal{F}[\Theta(r)] = \tilde{\Theta}(k)$ . Clearly, the inverse Fourier transformation of (A1) leads to

$$q = 0 \quad \text{and} \quad \Theta = 0. \tag{A2a,b}$$

Similarly, taking a Fourier transformation of (3.5a-c<sub>1,2</sub>), one obtains

$$k \cdot \tilde{v} = ih \quad \text{and} \quad \tilde{p}k + \tilde{\Pi} \cdot k = 0, \tag{A3a,b}$$

where from (2.5a,b<sub>1</sub>)

$$\tilde{\Pi} = iKn \left( \tilde{v}k + k\tilde{v} - \frac{2}{3} (k \cdot \tilde{v}) I \right). \tag{A4}$$

Equations (A3) and (A4) give

$$\tilde{v} = ih \frac{k}{|k|^2}, \quad \tilde{\Pi} = -2Knh \left( \frac{kk}{|k|^2} - \frac{1}{3} I \right), \quad \tilde{p} = \frac{4}{3} Knh. \tag{A5a-c}$$



	$\gamma_1$	$\gamma_2$	$d_1$	$d_4^*$	$C_4^*$
HS	1.27004	1.9223	2.4001	-0.4557	-2.1412
BGK	1	1	1.3027	-0.4467	-2.1320

Table 1. The values of  $\gamma_1$ ,  $\gamma_2$ ,  $d_1$ ,  $d_4^*$  and  $C_4^*$  for a hard-sphere gas (HS) and for the BGK model. Data taken from Sone (2007).

Finally, taking the inverse Fourier transformation of (A5) yields

$$\left. \begin{aligned} \mathbf{v} &= ih\mathcal{F}^{-1} \left[ \frac{\mathbf{k}}{|k|^2} \right] = \frac{h}{4\pi} \frac{\mathbf{r}}{|r|^3}, \quad p = 0, \quad \text{and} \\ \boldsymbol{\Pi} &= -2Kn h \mathcal{F}^{-1} \left[ \frac{\mathbf{k}\mathbf{k}}{|k|^2} - \frac{1}{3}\mathbf{I} \right] = \frac{3Kn h}{2\pi} \frac{1}{|r|^5} \left[ \mathbf{r}\mathbf{r} - \frac{1}{3}|r|^2\mathbf{I} \right]. \end{aligned} \right\} \quad (\text{A6a-c})$$

Here, we have used the following inverse Fourier transformation identities:

$$\mathcal{F}^{-1} \left[ \frac{\mathbf{k}}{|k|^2} \right] = -\frac{i}{4\pi} \frac{\mathbf{r}}{|r|^3} \quad \text{and} \quad \mathcal{F}^{-1} \left[ \frac{\mathbf{k}\mathbf{k}}{|k|^2} \right] = -\frac{3}{4\pi} \left[ \frac{\mathbf{r}\mathbf{r}}{|r|^5} - \frac{1}{3|r|^3}\mathbf{I} \right]. \quad (\text{A7a,b})$$

### Appendix B. Phenomenological coefficients in the boundary conditions

The numerical coefficients appearing in the phenomenological boundary conditions are based on Sone (2007), where these were obtained by an asymptotic expansion of the LBE for  $Kn \rightarrow 0$ . The coefficients  $\eta_{ij}$  appearing in (4.4a–c) can be directly compared with Sone (2007), as

$$\eta_{11} = -\frac{4\sqrt{\pi}d_1}{4C_4^*d_1 + 5\gamma_2d_4^*}, \quad \eta_{12} = \frac{5\sqrt{\pi}\gamma_2d_4^*}{4C_4^*d_1 + 5\gamma_2d_4^{*2}} \quad (\text{B1a,b})$$

$$\eta_{12} = -\frac{25\sqrt{\pi}\gamma_2^2d_4^{*2}}{16C_4^*d_1^2 + 20\gamma_2d_1d_4^{*2}} \quad \text{and} \quad \tau_0 = \frac{5\sqrt{\pi}\gamma_2}{8d_1}. \quad (\text{B2a,b})$$

Here, the values of  $\gamma_1$ ,  $\gamma_2$ ,  $d_1$ ,  $d_4^*$  and  $C_4^*$  for a hard-sphere gas (HS) and for the Bhatnagar–Gross–Krook (BGK) model are given in table 1.

### Appendix C. Analytic solutions obtained from fundamental solutions

The analytic solutions (6.1a–e) for an evaporating spherical droplet can also be obtained from the fundamental solutions (3.7a)–(3.7c). Owing to the spherical symmetry let us place one singular mass source of strength  $h$  and a heat source of strength  $g$  at the origin. Let  $\mathbf{r} = r\{\cos\phi\sin\theta, \sin\phi\sin\theta, \cos\theta\}$  be an arbitrary point outside the droplet ( $r \geq 1$ ). From (3.7) and (3.8) we get

$$\mathbf{v}(\mathbf{r}) \cdot \mathbf{n} = \frac{h}{4\pi r^2}, \quad p(\mathbf{r}) = 0, \quad \mathbf{n} \cdot \boldsymbol{\sigma}(\mathbf{r}) \cdot \mathbf{n} = \frac{Kn(h + \alpha_0 g Kn)}{\pi r^3} \quad (\text{C1a-c})$$

and

$$T(\mathbf{r}) = \frac{Pr}{c_p} \frac{g}{4\pi r}, \quad \mathbf{q}(\mathbf{r}) \cdot \mathbf{n} = \frac{Kng}{4\pi r^2} \quad (\text{C2a,b})$$

Comparing (C1) and (C2) with (6.1a–e), one finds  $c_1 = h/4\pi$  and  $c_2 = Kng/4\pi$ .

## REFERENCES

- ALLEN, M.D. & RAABE, O.G. 1982 Re-evaluation of Millikan's oil drop data for the motion of small particles in air. *J. Aerosol. Sci.* **13** (6), 537–547.
- BECKMANN, A.F., RANA, A.S., TORRILHON, M. & STRUCHTRUP, H. 2018 Evaporation boundary conditions for the linear R13 equations based on the Onsager theory. *Entropy* **20**, 680.
- BIRD, G.A. 1994 *Molecular Gas Dynamics and the Direct Simulation of Gas Flows*. Clarendon Press.
- BOBYLEV, A.V. 2006 Instabilities in the Chapman–Enskog expansion and hyperbolic Burnett equations. *J. Stat. Phys.* **124**, 371–399.
- BOND, M. & STRUCHTRUP, H. 2004 Mean evaporation and condensation coefficients based on energy dependent condensation probability. *Phys. Rev. E* **70**, 061605.
- CERCIGNANI, C. 2000 *Rarefied Gas Dynamics: From Basic Concepts to Actual Calculations*. Cambridge University Press.
- CERCIGNANI, C. & LORENZANI, S. 2010 Variational derivation of second-order slip coefficients on the basis of the boltzmann equation for hard-sphere molecules. *Phys. Fluids* **22** (6), 062004.
- CHAKRABORTY, S. & DURST, F. 2007 Derivations of extended Navier–Stokes equations from upscaled molecular transport considerations for compressible ideal gas flows: towards extended constitutive forms. *Phys. Fluids* **19** (8), 088104.
- CHANDRASHEKAR, P. 2013 Kinetic energy preserving and entropy stable finite volume schemes for compressible euler and Navier–Stokes equations. *Commun. Comput. Phys.* **14** (5), 1252–1286.
- CHENG, Y.-S., ALLEN, M.D., GALLEGOS, D.P., YEH, H.-C. & PETERSON, K. 1988 Drag force and slip correction of aggregate aerosols. *Aerosol. Sci. Technol.* **8**, 199–214.
- CHERNYAK, V.G. & MARGILEVSKIY, A.Y. 1989 The kinetic theory of heat and mass transfer from a spherical particle in a rarefied gas. *Intl J. Heat Mass Transfer* **32**, 2127–2134.
- CHUBYSKY, M.V., BELOUSOV, K.I., LOCKERBY, D.A. & SPRITTLES, J.E. 2020 Bouncing off the walls: the influence of gas-kinetic and van der Waals effects in drop impact. *Phys. Rev. Lett.* **124**, 084501.
- CLAYDON, R., SHRESTHA, A., RANA, A.S., SPRITTLES, J.E. & LOCKERBY, D.A. 2017 Fundamental solutions to the regularised 13-moment equations: efficient computation of three-dimensional kinetic effects. *J. Fluid Mech.* **833**, R4.
- DHAVALSWARAPU, H.K., MURTHY, J.Y. & GARIMELLA, S.V. 2012 Numerical investigation of an evaporating meniscus in a channel. *Intl J. Heat Mass Transfer* **55**, 915–924.
- DONGARI, N., CHAKRABORTY, S. & DURST, F. 2010 Predicting microscale gas flows and rarefaction effects through extended Navier–Stokes–Fourier equations from phoretic transport considerations. *Microfluid Nanofluid* **9**, 831–846.
- EU, B.C. 1992 *Kinetic Theory and Irreversible Thermodynamics*. Wiley.
- EVANS, L. 2000 *The Advent of Mechanical Refrigeration Alters Daily Life and National Economies throughout the World*, p. 537. Science and its times, Gale Group.
- FAN, C., CHEN, C. & MONROE, J. 2009 The method of fundamental solutions for solving convection-diffusion equations with variable coefficients. *Adv. Appl. Math. Mech.* **1** (2), 215–230.
- FREUND, R. & NACHTIGAL, N.M. 1991 QMR: a quasi-minimal residual method for non-Hermitian linear systems. *Numer. Math.* **60**, 315–339.
- FREZZOTTI, A., GROSFILS, P. & TOXVAERD, S. 2003 Evidence of an inverted temperature gradient during evaporation/condensation of a Lennard–Jones fluid. *Phys. Fluids* **15** (10), 2837–2842.
- GRAD, H. 1949a Note on  $N$ -dimensional Hermite polynomials. *Commun. Pure Appl. Maths* **2**, 325–330.
- GRAD, H. 1949b On the kinetic theory of rarefied gases. *Commun. Pure Appl. Maths* **2**, 331–407.
- GRAD, H. 1958 Principles of the kinetic theory of gases. In *Thermodynamik der Gase, Handbuch der Physik*, vol. 3/12, pp. 205–294. Springer.
- DE GROOT, S.R. & MAZUR, P. 1962 *Non-Equilibrium Thermodynamics*. North-Holland.
- GU, X.J. & EMERSON, D.R. 2007 A computational strategy for the regularized 13 moment equations with enhanced wall-boundary conditions. *J. Comput. Phys.* **225**, 263–283.
- GU, X.J. & EMERSON, D.R. 2009 A high-order moment approach for capturing non equilibrium phenomena in the transition regime. *J. Fluid Mech.* **636**, 177–216.
- GYARMATI, I. 1970 *Non-Equilibrium Thermodynamics*. Springer.
- HADJICONSTANTINO, N.G. 2003 Comment on Cercignani's second-order slip coefficient. *Phys. Fluids* **15** (8), 2352–2354.
- HARTEN, A. 1983 On the symmetric form of systems of conservation laws with entropy. *J. Comput. Phys.* **49**, 151–164.
- JIANG, X., WANG, X.G., BAI, Y.W. & PANG, C.T. 2014 The method of fundamental solutions for the moving boundary problem of the one-dimension heat conduction equation. In *Advanced Manufacturing and Automation*, vol. 1039, pp. 59–64. Trans Tech Publications Ltd.

- KJELSTRUP, S. & BEDEAUX, D. 2008 *Non-Equilibrium Thermodynamics of Heterogeneous Systems*. World Scientific.
- KREMER, G.M. 2010 *An Introduction to the Boltzmann Equation and Transport Processes in Gases*. Springer.
- KUMAR, H. & MISHRA, S. 2012 Numerical schemes for two-fluid plasma equations. *J. Sci. Comput.* **52**, 401–425.
- KUPRADZE, V.D. & ALEKSIDZE, M.D. 1964 The method of functional equations for the approximate solution of certain boundary value problems. *J. Comput. Math. Phys. USSR* **4**, 82–126.
- LAMB, H. 1945 *Hydrodynamics*, 6th edn. Dover.
- LEBON, G., JOU, D. & CASAS-VÁZQUEZ, J. 2008 *Understanding Non-Equilibrium Thermodynamics*. Springer.
- LIANG, Z., BIBEN, T. & KEBLINSKI, P. 2017 Molecular simulation of steady-state evaporation and condensation: validity of the Schrage relationships. *Intl J. Heat Mass Transfer* **114**, 105–114.
- LING, Z., ZHANG, Z., SHI, G., FANG, X., WANG, L., GAO, X., FANG, Y., XU, T., WANG, S. & LIU, X. 2014 Review on thermal management systems using phase change materials for electronic components, li-ion batteries and photovoltaic modules. *Renew. Sust. Energ. Rev.* **31**, 427.
- LIU, J., GOMEZ, H., EVANS, J.A., HUGHES, T.J. & LANDIS, C.M. 2013 Functional entropy variables: a new methodology for deriving thermodynamically consistent algorithms for complex fluids, with particular reference to the isothermal Navier–Stokes–Korteweg equations. *J. Comput. Phys.* **248**, 47–86.
- LOCKERBY, D.A. & COLLYER, B. 2016 Fundamental solutions to moment equations for the simulation of microscale gas flows. *J. Fluid Mech.* **806**, 413–436.
- LOPES, D.S., SILVA, M.T. & AMBRÓSIO, J.A. 2013 Tangent vectors to a 3-d surface normal: a geometric tool to find orthogonal vectors based on the householder transformation. *Comput.-Aided Des.* **45**, 683–694.
- MCELROY, P.J. 1979 Surface tension and its effect on vapor pressure. *J. Colloid Interface Sci.* **72** (1), 147–149.
- MCGAUGHEY, A.J.H. & WARD, C.A. 2002 Temperature discontinuity at the surface of an evaporating droplet. *J. Appl. Phys.* **91** (10), 6406–6415.
- MILLIKAN, R.A. 1923 Coefficients of slip in gases and the law of reflection of molecules from the surfaces of solids and liquids. *Phys. Rev.* **21** (3), 217–238.
- MÜLLER, I. & RUGGERI, T. 1998 *Rational Extended Thermodynamics*. Springer.
- MYONG, R.S. 2014 On the high Mach number shock structure singularity caused by overreach of Maxwellian molecules. *Phys. Fluids* **26** (5), 056102.
- ONSAGER, L. 1931 Reciprocal relations in irreversible processes. II. *Phys. Rev.* **38**, 2265–2279.
- ÖTTINGER, H. 2010 Thermodynamically admissible 13 moment equations from the Boltzmann equation. *Phys. Rev. Lett.* **104**, 120601.
- PAO, Y. 1971 Application of kinetic theory to the problem of evaporation and condensation. *Phys. Fluids* **14** (2), 306–312.
- PAOLUCCI, S. & PAOLUCCI, C. 2018 A second-order continuum theory of fluids. *J. Fluid Mech.* **846**, 686–710.
- PLAWSKY, J.L., FEDOROV, A.G., GARIMELLA, S.V., MA, H.B., MAROO, S.C., CHEN, L. & NAM, Y. 2014 Nano- and microstructures for thin-film evaporation—a review. *Nanoscale Microscale Thermophys. Engng* **18**, 251–269.
- RANA, A.S., GUPTA, V.K. & STRUCHTRUP, H. 2018a Coupled constitutive relations: a second law based higher-order closure for hydrodynamics. *Proc. R. Soc. Lond. A* **474**, 20180323.
- RANA, A.S., LOCKERBY, D.A. & SPRITTLES, J.E. 2018b Evaporation-driven vapour microflows: analytical solutions from moment methods. *J. Fluid Mech.* **841**, 962–988.
- RANA, A.S., LOCKERBY, D.A. & SPRITTLES, J.E. 2019 Lifetime of a nanodroplet: kinetic effects and regime transitions. *Phys. Rev. Lett.* **123**, 154501.
- RANA, A.S. & STRUCHTRUP, H. 2016 Thermodynamically admissible boundary conditions for the regularized 13 moment equations. *Phys. Fluids* **28**, 027105.
- SARNA, N. & TORRILHON, M. 2018 On stable wall boundary conditions for the Hermite discretization of the linearised Boltzmann equation. *J. Stat. Phys.* **170**, 101–126.
- SCHRAGE, R.W. 1953 *A Theoretical Study of Interphase Mass Transfer*. Columbia University Press.
- SCHWEIZER, M., ÖTTINGER, H.C. & SAVIN, T. 2016 Nonequilibrium thermodynamics of an interface. *Phys. Rev. E* **93**, 052803.
- SHERWOOD, L. 2005 *Fundamentals of Physiology: A Human Perspective*. Brooks/Cole.
- SONE, Y. 2007 *Molecular Gas Dynamics: Theory, Techniques, and Applications*. Birkhäuser.
- SONE, Y., TAKATA, S. & WAKABAYASHI, M. 1994 Numerical analysis of a rarefied gas flow past a volatile particle using the Boltzmann equation for hard-sphere molecules. *Phys. Fluids* **6**, 1914.
- SPRITTLES, J.E. & SHIKHMURZAEV, Y.D. 2012 The dynamics of liquid drops and their interaction with solids of varying wettabilities. *Phys. Fluids* **24**, 082001.

- STIMSON, M., JEFFERY, G.B. & FILON, L.N.G. 1926 The motion of two spheres in a viscous fluid. *Proc. R. Soc. Lond. A* **111** (757), 110–116.
- STRUCHTRUP, H. 2005 *Macroscopic Transport Equations for Rarefied Gas Flows*. Springer.
- STRUCHTRUP, H., BECKMANN, A., RANA, A.S. & FREZZOTTI, A. 2017 Evaporation boundary conditions for the R13 equations of rarefied gas dynamics. *Phys. Fluids* **29**, 092004.
- STRUCHTRUP, H. & NADLER, B. 2020 Are waves with negative spatial damping unstable? *Wave Motion* **97**, 102612.
- STRUCHTRUP, H. & TORRILHON, M. 2007  $h$  theorem, regularization, and boundary conditions for linearized 13 moment equations. *Phys. Rev. Lett.* **99**, 014502.
- STRUCHTRUP, H. & TORRILHON, M. 2008 Higher-order effects in rarefied channel flows. *Phys. Rev. E* **78**, 046301.
- STRUCHTRUP, H. & TORRILHON, M. 2010 Comment on “Thermodynamically admissible 13 moment equations from the Boltzmann equation”. *Phys. Rev. Lett.* **105**, 128901.
- TADMOR, E. & ZHONG, W. 2006 Entropy stable approximations of Navier–Stokes equations with no artificial numerical viscosity. *J. Hyperbol. Differ. Eq.* **03** (03), 529–559.
- TAKATA, S., SONE, Y., LHUILLIER, D. & WAKABAYASHI, M. 1998 Evaporation from or condensation onto a sphere: numerical analysis of the Boltzmann equation for hard-sphere molecules. *Comput. Maths Applics.* **35**, 193–214.
- TORRILHON, M. 2012 H-Theorem for nonlinear regularized 13-moment equations in kinetic gas theory. *Kinet. Relat. Mod.* **5**, 185–201.
- TORRILHON, M. 2016 Modeling nonequilibrium gas flow based on moment equations. *Annu. Rev. Fluid Mech.* **48**, 429–458.
- TORRILHON, M. & SARNA, N. 2017 Hierarchical Boltzmann simulations and model error estimation. *J. Comput. Phys.* **342**, 66–84.
- TORRILHON, M. & STRUCHTRUP, H. 2008 Boundary conditions for regularized 13-moment equations for micro-channel-flows. *J. Comput. Phys.* **227**, 1982–2011.
- WARD, C.A. & FANG, G. 1999 Expression for predicting liquid evaporation flux: statistical rate theory approach. *Phys. Rev. E* **59**, 429–440.
- ZINNER, C.P. & ÖTTINGER, H.C. 2019 Entropic boundary conditions for 13 moment equations in rarefied gas flows. *Phys. Fluids* **31** (2), 021215.